Organic Geochemistry 201 (2025) 104918

Contents lists available at ScienceDirect

Organic Geochemistry

journal homepage: www.elsevier.com/locate/orggeochem

Study on the main controlling factors on the differential accumulation of natural gas in multiple (ultra-)deeply-buried marine strata☆

Zezhang Song [a,b,*], Ziyu Zhang [a,b], Bing Luo [c,d,**], Wenjin Zhang [c,d], Changqi Liu [a,b], Xingwang Tian [c,d], Dailin Yang [c,d], Luya Wu [c,d], Bingfei Ge [a,b], Shigui Jin [a,b], Jiutao Yuan [a,b]

[a] *National Key Laboratory of Petroleum Resources and Engineering, China University of Petroleum (Beijing), Beijing 102249, China*
[b] *College of Geosciences, China University of Petroleum (Beijing), Beijing 102249, China*
[c] *PetroChina Southwest Oil & Gas Field Company, Chengdu, Sichuan, China*
[d] *Research Institute of Petroleum Exploration & Development in PetroChina Southwest Oil & Gas Oilfield Company, Chengdu, Sichuan 610051, China*

A R T I C L E I N F O

Executive Guest Editor — Huiyuan Xu

Keywords:
Ultra-deeply buried strata
Marine carbonate natural gas
Multiple strata
Gas-source correlation
Differential accumulation

A B S T R A C T

Ultra-deep natural gas is characterized by significant burial depth, high maturity, limited biomarkers, and complicated gas-source relationships. Ultra-deep gas accumulations generally underwent complex modifications during their long evolution, making it challenging to clarify the controlling factors of gas accumulation. This study focuses on gas accumulations in multiple (ultra-)deep marine carbonate strata, ranging from the Sinian Dengying (Z_2dn) to the Permian Maokou (P_2m) formations, in the Penglai gas area of the central Sichuan Basin. Using unsupervised machine learning algorithms, we conducted clustering analysis on natural gas composition and isotopes ($\delta^{13}C$ and δ^2H). Furthermore, we combined reservoir microscopic analysis, isotope data ($\delta^{13}C$ of kerogen and solid bitumen; and $\delta^{18}O$, $\delta^{13}C$, and $^{87}Sr/^{86}Sr$ of dolomite), and fluid inclusion analysis to determine the main controlling factors that differentiate gas accumulation in multiple marine carbonate strata. The results indicate that: (1) Natural gases from Z_2dn-P_2m strata in the Penglai gas area are mainly dry gas (dryness > 0.996). Specifically, Z_2dn natural gas exhibits high non-hydrocarbon content, low C_2H_6, $\delta^{13}C_{C_2H_6}$, and $\delta^2H_{CH_4}$. Conversely, the Cambrian (Є) natural gas demonstrates the opposite characteristics. The natural gas in P_2m has relatively high C_2H_6, greater $\delta^{13}C_{C_2H_6}$ and $\delta^2H_{CH_4}$ values. (2) The natural gas from Z_2dn-P_2m in the Penglai gas area is oil-cracking gas and mainly sourced from $Є_1$q. Due to maturity, hydrocarbon gases are dominated by CH_4. He and N_2 are from inorganic, deep Earth sources and show differential enrichment. Influenced by hydrothermal alteration and TSR, H_2S and CO_2 are enriched in Z_2dn. The $\delta^{13}C_{C_2H_6}$ in natural gas follows the order: Z_2dn > P_2m > Cambrian. The $\delta^{13}C_{CH_4}$ in natural gas follows the order: Z_2dn ≥ P_2m > Cambrian. (3) Overall, the Z_2dn-P_2m differential accumulation in the Penglai gas area is primarily influenced by various factors, including multiple source rocks, deep hydrothermal transformation, and strike-slip faults.

1. Introduction

In the past three years, the PetroChina Southwest Oil & Gas Field Company has made significant breakthroughs in the (ultra-) deep gas exploration in marine carbonate on the North Slope of the central Sichuan Paleo-uplift (Wang et al., 2022a). As of September 2022, industrial gas flows had been discovered in the second member (Z_2dn^2, in well PT1, May 4, 2020, 121.98 × 10^4 m^3/d, gas test in 5730 m–5810 m) and the fourth member (Z_2dn^4, in well DB1, February 2022, 28.54 × 10^4 m^3/d, gas test in 6312 m–6484 m and 6537 m–6684 m) of the Dengying Formation (Z_2dn), the Cambrian Canglangpu Formation ($Є_1$c, in well JT1, October 16, 2020, 51.62 × 10^4 m^3/d, gas test in 6972 m–6993 m and 7006 m–7026 m), the Cambrian Longwangmiao Formation ($Є_1$l, in well DB1, September 2022, 20.28 × 10^4 m^3/d, gas test in 5728 m–5758 m, 5764 m–5773 m) and the Permian Maokou Formation (P_2m, in well JT1, 112.8 × 10^4 m^3/d, gas test in 6155 m–6175 m). Successful gas

☆ This article is part of a special issue entitled: Xplorer, hybrid and early-career' published in Organic Geochemistry.

* Corresponding author at: National Key Laboratory of Petroleum Resources and Engineering, China University of Petroleum (Beijing), Fuxue Road No. 18, Changping, Beijing 102249, China.
** Corresponding author at: Research Institute of Exploration and Development, PetroChina Southwest Oil & Gas Field Company, Sichuan 610041, China.
E-mail addresses: songzz@cup.edu.cn (Z. Song), lb2001@petrochina.com.cn (B. Luo).

https://doi.org/10.1016/j.orggeochem.2024.104918
Received 3 June 2024; Received in revised form 15 December 2024; Accepted 16 December 2024

exploration of the Sinian-Permian system in multiple strata of marine carbonate gas on the North Slope of the central Sichuan paleo-uplift is clear (Song et al., 2024; Yang et al., 2022; Zhang et al., 2023a). The Penglai gas area is assessed to contain proven natural gas reserves of 2065.43×10^8 m^3 in Z_2dn^2 and predicted natural gas reserves of 3812.48×10^8 m^3 in Z_2dn^4, 1524.49×10^8 m^3 in $Є_1c$, and 3015.21×10^8 m^3 in P_2m.

Knowledge of natural gas molecular and stable and rare gas isotopic composition is crucial to studying its origin, source, and secondary modification processes (migration, gas-mixing, biodegradation, etc.) (Liu et al., 2019; Milkov and Etiope, 2018; Wu et al., 2019). Geochemical characteristics (composition and isotopes) of gases in the Sinian-Permian multiple carbonate strata vary greatly (Liang et al., 2019; Wei et al., 2022). From a compositional standpoint, the Sinian gas reservoirs exhibit relatively higher contents of non-hydrocarbon gases, while the Cambrian $Є_1c$, $Є_1l$, and the Permian P_2m gases display lower levels of non-hydrocarbon gases and higher levels of hydrocarbons. Furthermore, subtle disparities exist in the natural gas constituents between the Cambrian and Permian gas reservoirs. From an isotopic perspective, an "inversion" in carbon isotopes (i.e., the stable carbon isotope of methane ($\delta^{13}C_{CH_4}$) higher than ethane ($\delta^{13}C_{C_2H_6}$)) is prevalent in both Cambrian and Permian gas reservoirs. In contrast, the carbon isotope of natural gases in Sinian reservoirs adheres to a regular pattern. $\delta^{13}C_{C_2H_6}$ is a good indicator of the parent source (Dai, 1993). The $\delta^{13}C_{C_2H_6}$ of the natural gas from $Є_1l$ in the Gaoshiti-Moxi area and the North Slope is typical of oil-type gas (− 35.3 ‰ to −30.6 ‰), significantly lower than that of the natural gas from Z_2dn (–33.6 ‰ to −26.0 ‰) (Zhao et al., 2021). It is worth noting that the $\delta^{13}C_{C_2H_6}$ distribution of Z_2dn is broader, covering part of the range associated with coal-derived gases. While predecessors have conducted extensive research on the origin and source of natural gas in the Penglai gas area of the central Sichuan Basin, there are still differences in the interpretation of its geochemical characteristics.

1.1. Differences in the genetic type of gases

Multiple possible source rocks are present in the Sinian-Permian system of the Sichuan Basin. Potential source rocks include black shales in the third member of the Sinian Dengying Formation (Z_2dn^3) and the Lower Cambrian Qiongzhusi/Maidiping Formation ($Є_1q$), and the Middle Permian Maokou (P_2m) to Qixia (P_2q) formations including bright-micrite bioclastic limestone, OM-rich micrite bioclastic limestone (eyeball limestone) and argillaceous rocks. (Xie et al., 2021b). Due to the influence of the Caledonian and Yunnan movements, the Silurian Longmaxi Formation, Devonian, and Carboniferous were eroded in the Penglai gas area (Li et al., 2022).

The organic matter type of Z_2dn^3 and $Є_1q$ is sapropel; in contrast, the OM in P_2m-P_2q is a sapropel-humic mixed (sapropel type dominates) (Xie et al., 2021b). In addition, the redox conditions of the source rock's depositional environment are quite different – the depositional environment of the $Є_1q$ is more reduced, while that of Z_2dn^3 is more oxidizing (Zhu et al., 2022). In the Anyue Gas Field, the Z_2dn^2 and Z_2dn^4 gases are mainly derived from the $Є_1q$, with a partial contribution of the Z_2dn^3 (Xie et al., 2021b); the natural gas of the $Є_1l$ and $Є_1c$ generally are derived from the $Є_1q$ (Zhao et al., 2021). The natural gas in the P_2m beyond the Silurian pinch-out line is primarily from the $Є_1q$ source, with a partial contribution from the P_2m-P_2q source rocks. Within this pinch-out line, P_2m gas composition includes contributions from the Longmaxi shale, expanding its source complexity (Xie et al., 2020).

1.2. Differences in maturity of source rocks

Source rock maturity varies across different strata: the Z_2dn^3 source rock exhibits higher maturity levels ($R_o = 3.16$ % to 3.21 %) compared to the $Є_1q$ ($R_o = 2.42$ %) and the P_2m-P_2q (R_o >2.2 %) (Wang et al., 2022b; Wei et al., 2015). Additionally, maturity varies within the same formation at different locations; for instance, the maturity of $Є_1q$ source rocks in the Weiyuan gas field is lower than in the Anyue gas field (Shuai et al., 2021). $\delta^{13}C_{CH_4}$ and $\delta^{13}C_{C_2H_6}$ generated from these rocks exhibit distinct trends with maturity: $\delta^{13}C_{CH_4}$ typically becomes greater as maturity increases; $\delta^{13}C_{C_2H_6}$ initially becomes greater, then lower, and greater again (Wu et al., 2016b). At high maturities, a decrease in $\delta^{13}C_{C_2H_6}$ will lead to the inversion of natural gas isotopes. However, in the over-mature stage, Rayleigh distillation occurs; as maturity rises, $\delta^{13}C_{C_2H_6}$ incrementally becomes greater due to diminishing C_2H_6 content with a more pronounced shift than $\delta^{13}C_{CH_4}$, potentially reverting the isotopic signature to a non-inverted state. Consequently, some researchers argue that variations in the natural gas of Z_2dn^2, Z_2dn^4, and Cambrian accumulations arise from differing maturities rather than source rock distinctions (Wu et al., 2016b).

1.3. Differences in gas genesis

Ultra-deep marine carbonate gas reservoirs, undergoing multiple tectonic movements, have experienced transitions from paleo-oil reservoirs to paleo-gas reservoirs and, ultimately, to current gas reservoirs (Song et al., 2021). It is well-acknowledged that the Sinian-Permian natural gas in the Anyue gas field predominantly belongs to oil-cracking gas due to the *in situ* cracking of paleo-oil-reservoirs (Wu et al., 2016a; Xie et al., 2021a). This theory, however, does not adequately account for the observation that the $\delta^{13}C_{CH_4}$ of natural gas in the Z_2dn and $Є_1l$ exhibit greater values than those of solid bitumen $\delta^{13}C$ within these reservoirs. Therefore, several mechanisms should be considered to elucidate the origins of natural gas.

1.3.1. Kerogen thermal degradation

Based on isotope fractionation principles, Shuai et al. (2023) argued that natural gas accumulation in Z_2dn^2 and Z_2dn^4 reservoirs is influenced by the mix of oil-cracked gas and late-stage kerogen-cracked gas, resulting in natural gas with greater carbon isotopes than reservoir solid bitumen produced by early-stage crude oil cracking. Conversely, $Є_1l$ and $Є_1c$ reservoirs primarily contain oil-cracked gas, while late-stage kerogen-cracked gas predominantly characterizes the Permian natural gas.

1.3.2. Residual bitumen cracking gas

The primary migration for hydrocarbons from sapropel organic matter is generally early and efficient. Nonetheless, highly mature source rocks still retain a considerable amount of residual bitumen (Chen et al., 2017), which can crack in situ, contributing significantly to gas generation — up to 68.2 % in high-maturity source rocks (He et al., 2013).

1.3.3. Dissolved gas precipitation

$\delta^{13}C_{CH_4}$ of water-soluble gas released from gas field water are greater than those in the reservoir's free natural gas. This discrepancy might be due to degassing from the water-soluble phase in formation water (Qin et al., 2016), particularly evident in $Є_1l$ – $\delta^{13}C_{CH_4}$ is greater than that of reservoir solid bitumen

1.4. Modification by thermal anomalies

The Sichuan Basin's Middle to Late Permian epoch was marked by intense volcanic activity during the Dongwu movement, forming massive Emeishan Basalt and associated thermal anomalies. These anomalies accelerated paleo-oil-reservoir cracking (Fang et al., 2024; Zhu et al., 2022). Furthermore, sulfate thermochemical reduction (TSR) processes generate carbon dioxide (CO_2) and hydrogen sulfide (H_2S), significantly altering natural gas compositions (Liu et al., 2016; Shuai et al., 2019). Hydrothermal activity can transport SO_4^{2-} from deep Earth, supplying sulfur for TSR reactions (Zhang, 2019; Zhu et al., 2021). Strong TSR reactions alter gas compositions and affect carbon isotopes

(Liu et al., 2012), resulting in greater residual $\delta^{13}C_{C_2H_6}$ (Shuai et al., 2019).

1.5. Effects of deep inorganic gas sources

The Z_2dn natural gas has a high content of non-hydrocarbon gases, including helium (He), nitrogen (N_2), and others (Wei et al., 2015). The Sichuan Basin has a uranium- and thorium-rich granite basement (Zhang et al., 2023b). Є$_1$q source rock exhibits high maturity and radioactivity (Zhao et al., 2016), which can serve as a source of helium and nitrogen (Xie et al., 2021b). Natural gas and paleo-formation water also can serve as migration carriers for He and N_2. Deep strike-slip faults are common in the central Sichuan basin, providing conduits and migration channels for deep inorganic gas.

In summary, the distinct geochemical characteristics of Sinian-Permian ultra-deep natural gas come from a myriad of factors, including source, maturity, inorganic gas genesis, and secondary modification processes. This study will focus on comparing the Sinian-Permian multi-strata natural gas accumulation (Z_2dn^2, Z_2dn^4, Є$_1$c, Є$_1$l, and P_2m) in the Penglai gas area to clarify the causes of these differences. This objective will be pursued using unsupervised machine learning techniques to compare and analyze the geochemical characteristics of natural gas; after clarifying the geochemical characteristics of solid bitumen, we will carry out gas-bitumen-source correlation to establish natural gas accumulation modes for ultra-deep multi-strata.

2. Geologic settings

The Penglai gas area is situated in the central Sichuan Basin, within the monoclinic tectonic zone, north of the core of the Leshan-Longnvsi Caledonian paleo-uplifts and adjacent to the Deyang-Anyue rift trough to the west (Fig. 1a). Sinian to Permian marine carbonate strata have developed multiple sets of source rocks (Fig. 1b), including the Sinian Z_2dn^3 Member, the Lower Cambrian Є$_1$q, the Permian Liangshan Formation, P_2m-P_2q and the Longtan Formation. The Lower Cambrian Є$_1$q is considered to be the primary source rock, extensively overlying and distributed across the basin. The Deyang-Anyue rift trough acts as the centre of hydrocarbon generation, where Є$_1$q has a thickness of 250 m–300 m (Li et al., 2024; Xie et al., 2020). The Sinian-Permian accumulations in the Penglai gas area encompass several reservoir sets, namely the Upper Sinian Z_2dn^2 and Z_2dn^4, Lower Cambrian Є$_1$c and Є$_1$l, Upper Cambrian Xixiangchi Formation(Є$_3$x), and Permian P_2m (Fig. 1b).

3. Sampling and methods

Gas samples were obtained from the Sinian Z_2dn^2, Z_2dn^4, Cambrian Є$_1$l, Є$_1$c, Є$_3$x, and Permian P_2m formations of the Penglai Gas Field in the central Sichuan Basin by the Research Institute of Petroleum Exploration & Development of PetroChina Southwest Oil & Gas Oilfield Company. Collection was conducted using a double-valve high-pressure cylinder (10 cm diameter, approximately 1000 cm^3 volume) fitted with a shut-off valve capable of withstanding up to 22.5 MPa. The cylinder pressure was kept above 5.0 MPa to ensure sample integrity. The samples were taken directly from the wellhead to minimize air exposure, following a 15–20 min purge with the target gas to eliminate any air contaminants before sampling commenced. Following collection, the cylinders were thermally stabilized in a water bath and checked for potential leaks.

The Research Institute of Petroleum Exploration & Development in PetroChina Southwest Oil & Gas Oilfield Company provided rock samples. Reservoir samples were collected from P_2m, Є$_1$c and Є$_1$l in the Penglai gas area of the central Sichuan Basin. Source rock samples were collected from Z_2dn^3 and Є$_1$q (black shales) and P_2m-P_2q (OM–rich

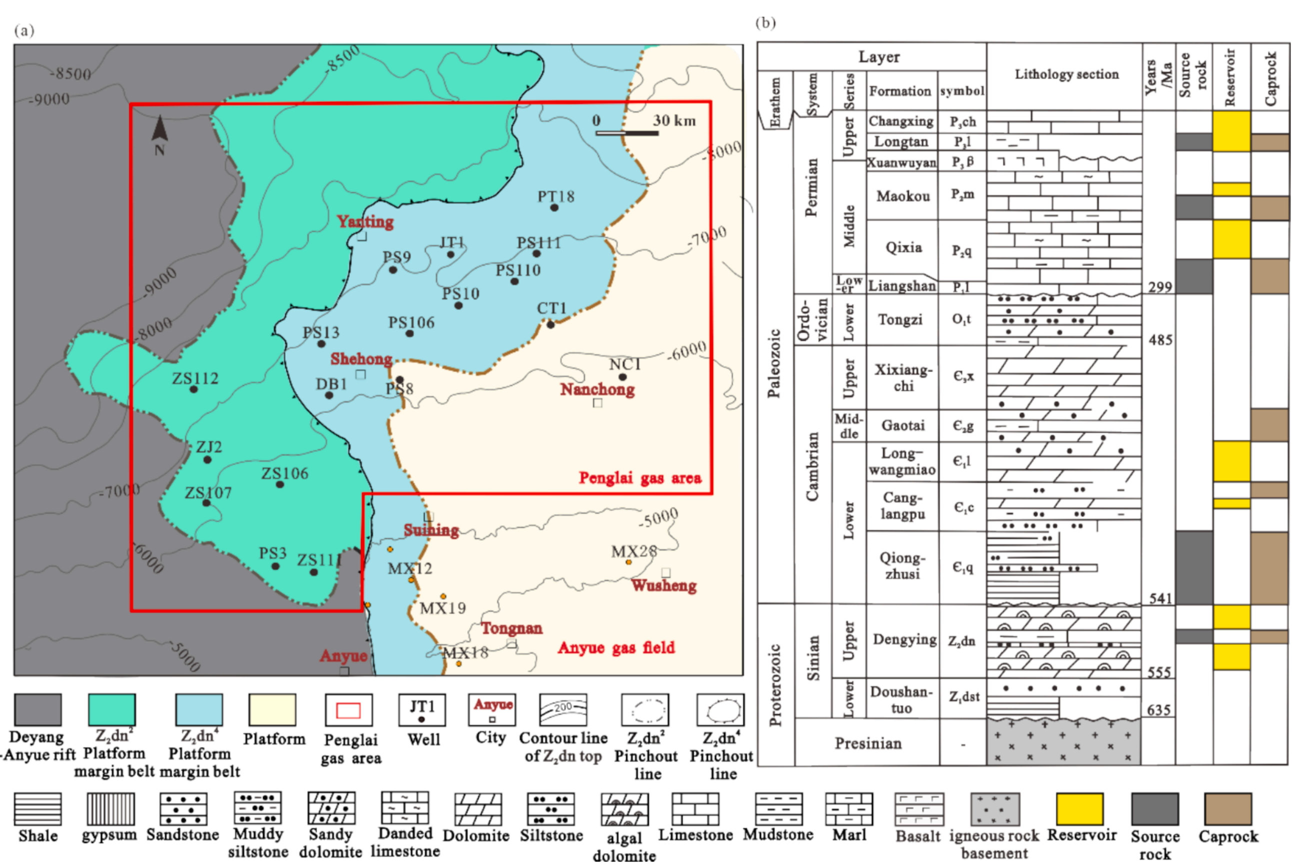

Fig. 1. Geologic background(a) and stratigraphic column(b) of Sinian – Permian system in Penglai gas area ((a) Contour line indicator Z_2dn top altitude; (b) Modified from(Xie et al., 2021).

micrite bioclastic limestone samples). Additionally, core samples of Z_2dn^2, Z_2dn^4 were obtained from wells PS3, PS4, PT1, PT101, and PT102. Dolomite samples were polished on both sides to a thickness of about 0.03 mm for thin section observation and about 0.2 mm for fluid inclusion observation and laser Raman measurement. The dolomite rock samples were ground to a particle size of 20–40 mesh and then ultrasonically cleaned, air-dried, and further ground into a powder finer than 200 mesh to conduct geochemical analysis.

Preparation of solid bitumen from P_2m, $Є_1c$, $Є_1l$ and Z_2dn reservoir rocks involves the following steps: First, dolomite containing solid bitumen was crushed into small pieces of 3 mm to 5 mm. Next, use wooden tools to select the solid bitumen granules shaken out and then observed with a 10x microscope to select pure solid bitumen granules. Subsequently, these selected solid bitumen samples were placed in a cup of anhydrous ethanol, washed in an ultrasonic bath, and then dried. Finally, the solid bitumen is ground to 200 mesh.

Preparation of kerogen involves the following steps: 6 mol/L HCl was added to the residual rock powder (Z_2dn^3, $Є_1q$ and $P_2m - P_2q$) after extraction to fully decompose the carbonate rocks then rinsed. 6 mol/L HCl and 40 % HF by mass were then added to decompose the siliceous rocks fully, then rinsed. Next, a heavy liquid with a relative density of 2.0–2.1 g/cm^3 was added and an enriched kerogen fraction was obtained by flotation in a high-speed centrifuge. Finally, 6 mol/L HCl was added and reacted with arsenic-free zinc granules. After no H_2S odor was detected, heavy liquid flotation was used to remove impurities and eliminate pyrite from the kerogen. A final wash with distilled water followed by freeze-drying obtained purified kerogen.

The Analytical Experiment Center of the Exploration and Development Research Institute, PetroChina Southwest Oil & Gas Field Company, conducted natural gas composition and isotope analyses. The natural gas composition was analyzed using an Agilent 6890 N gas chromatograph (GC) following GB/T 13610–2020 testing standards. For the carbon isotope analysis of natural gas, an Optima gas isotope ratio mass spectrometer coupled with a Hewlett-Packard 6890 II gas chromatograph was employed to measure the stable carbon isotope values of the gas samples by SY/T 5238–2008. The hydrocarbon gas composition was separated using a fused silica capillary column (30 m × 0.32 mm), with the oven temperature programmed to rise from 35 °C to 80 °C at a rate of 8 °C/min, then to 260 °C at a rate of 5 °C/min, and held for 10 min. Eluted hydrocarbons were converted to CO_2 by on-line combustion for carbon isotope measurements. The hydrogen isotope analysis of natural gas was implemented under SY/T 7313–2016. CH_4 was converted to H_2, and the hydrogen isotope ratios were measured using a Finnigan Mat Delta S mass spectrometer linked to an HP 5890II chromatograph. The hydrocarbon stable isotope ratios were assessed relative to the VPDB and V-SMOW standards. Gas isotope ratios are reported as "δ" in " ‰", with $\delta^{13}C$ and δ^2H_{CH4} measured with an accuracy of ± 0.1 ‰ and ± 1.0 ‰, respectively.

Petrographic analysis was conducted at the National Key Laboratory of Petroleum Resources and Engineering, China University of Petroleum (Beijing). A Leica DM 4500P microscope CL8200 MK5 cathodoluminescence microscope was used, with working conditions of 7–10 kV and 400–500 mA, and a DFC 450C camera observed the microscopic characteristics of dolomite and hydrothermal minerals.

The Key Laboratory of Reservoir Description of CNPC conducted the analysis and testing of carbon and oxygen isotopes as well as strontium isotopes in carbonate rocks. The carbon and oxygen isotopes were analyzed by a Thermo Fisher DELTA V Advantage isotope ratio mass spectrometer following the SY/T 5238–2019 standard. The sealed reaction vial containing a powdered sample was evacuated with high-purity helium gas. Subsequently, 6 to 8 drops of anhydrous phosphoric acid were injected and the reaction was carried out at a constant temperature of 70 °C for 1 h. The CO_2 gas released during the process was carried into the isotope mass spectrometer by a helium gas flow. The $\delta^{13}C$ and $\delta^{18}O$ values obtained are expressed relative to the VPDB standard.

The strontium isotopes were analyzed following the GB/T 17672–1999 "strontium isotope analysis methods for and carbonate rocks". The testing environment had a relative humidity of 20 % and a temperature of 20°C. Dolomite powder was dissolved in HCl solution and reacted thoroughly at 100°C to 110°C. Strontium was extracted using an AG 50WX12 ion exchange resin column, and the $^{87}Sr/^{86}Sr$ ratio was determined using a Triton plus mass spectrometer (Isoprobe-T thermal ionization mass spectrometer).

Laser Raman experiments on inclusions were conducted at China University of Petroleum (Beijing) using a LABHR −VIS LabRAM HR800 high-grade micro laser Raman spectrometer equipped with a Yag crystal frequency-doubled solid-state laser. The experiments were conducted under the SY/T 7662–2022 standard. This spectroscopy technique is well-suited for identifying molecular species within inclusions, particularly in geological samples. The instrument's settings allowed for a scanning range from 100 cm^{-1} to 4200 cm^{-1}, with a laser wavelength of 532 nm, providing detailed spectral information critical for the characteristics of the gas components within the inclusions.

The carbon isotopes of solid bitumen and kerogen were analyzed at the National Key Laboratory of Petroleum Resources and Engineering, China University of Petroleum (Beijing), using a Finnigan MAT 253 isotope mass spectrometer. The results were standardized using the VPDB standard (‰). The precision of the analysis was ensured through repeated measurements of laboratory standard samples, with an accuracy better than 0.1 ‰.

The hierarchical clustering algorithm assumes that each data point is initially a separate cluster, and in each iteration of the algorithm, it identifies the clusters with high similarity and merges them. This process is repeated iteratively until only one cluster remains. Compared to other clustering algorithms, hierarchical clustering does not require the pre-specification of the number of clusters and can explore the hierarchical relationships between clusters and the algorithm's workflow can be visualized using a dendrogram. Hierarchical clustering does not involve metadata. In our Python analysis, we conduct cluster analysis with two parameters each time. Despite having only two variables, the emphasis in hierarchical clustering is on the similarity or distance between sample data. As a result, clustering algorithms can still reveal potential structures and patterns within the data. Therefore, we analyze the genetic differences of natural gas based on the relationships between different clusters.

4. Result

4.1. Molecular composition of natural gases

In the Penglai gas area, the composition of natural gases within the Sinian-Permian multi-strata exhibits distinct variations. Hydrocarbon gases are present predominantly, with differing non-hydrocarbon gases across different strata (Table 1).

Sinian natural gas is characterized by high levels of non-hydrocarbons and low hydrocarbons, with elevated H_2S, N_2, He, and CO_2 alongside relatively low CH_4 and C_2H_6 contents. In contrast, Cambrian natural gas is rich in hydrocarbons, predominantly CH_4, though some samples show elevated CO_2 content. Permian natural gas, predominantly CH_4, shows relatively higher C_2H_6 levels and increased CO_2 contents than Cambrian (Table 1).

4.1.1. Hydrocarbon gas composition

The hydrocarbon gases within the Z_2dn^2 and Z_2dn^4 are predominantly CH_4, ranging from 6.57 % to 94.94 % of the total gas, with a broad distribution, accompanied by minimal C_2H_6 at 0.09 % to 0.01 %. These gases exhibit the highest dryness, with most values exceeding 0.999 (Table 1). In contrast, the hydrocarbon gases of the $Є_1l$, $Є1c$, and $Є_3x$ formations show elevated overall CH_4 content (79.07 %–98.01 %) and slightly higher C_2H_6 levels (0.12 %–0.21 %), with dryness between 0.997 and 0.999, though the dryness of $Є_1c$ natural gas are somewhat

Table 1
Chemical and isotopic compositions of natural gas in Sinian – Permian system in Penglai gas area.

Block	Well	Depth/m	Formation	Main composition / %							H_2S content	$\delta^{13}C$ / ‰			$\delta^2H_{CH_4}$ / ‰	Source
				He	H_2	N_2	CO_2	H_2S	CH_4	C_2H_6	(g/m^3)	$\delta^{13}C_{CH_4}$	$\delta^{13}C_{CO_2}$	$\delta^{13}C_{C_2H_6}$		
Zhongjiang block	ZJ2	5048	P_3ch	0.01	0.01	0.53	4.56	0.65	94.06	0.18	13.00	−33.6	–	−32.7	−140	1
JT1 block	JT1	6155–6175	P_2m	0.03	0.00	0.16	11.50	0.12	87.93	0.25	1.70	−27.7	2.2	−32.8	−135	1
	JT1	6165	P_2m	0.01	0.01	0.21	14.09	0.11	85.34	0.23	1.70	−32.4	–	−33.3	−134	1
Zhongjiang block	ZJ1	5605	P_2m	0.01	0	0.34	2.32	0.03	97.14	0.16	0.56	−35.0	–	−34.0	−136	1
Nanchong block	NC1	5045	P_2m	0.02	0.15	0.24	2.18	1.71	95.57	0.13	25.94	−30.9	–	−31.1	−133	2
	NC3	6010	P_2m	0.02	0.05	0.13	4.93	1.55	93.16	0.16	23.35	−30.3	–	−31.3	−125	2
PT1 block	PT103	4663–4691	P_2m	0.01	0.03	0.53	10.95	0.08	88.07	0.32	1.16	−30.6	4.0	−33.1	−137	1
Nanchong block	NC1	5447	$Є_3x$	0.01	0.39	0.34	2.54	0.02	96.57	0.13	0.36	−33.6	–	−32.5	−135	1
	NC1	6264	$Є_3x$	0.01	0.23	0.38	5	0.04	94.13	0.21	0.661	−35.8	–	−36.6	−136	1
DB1 block	PS13	6080–6095	$Є_1l$	0.01	0.13	0.42	11.4	0.36	87.48	0.19	5.19	−36.8	−3.4	−38.1	−137	1
JT1 block	JT1	6852.5–7032.0	$Є_1c$	0.02	0.03	0.31	1.26	0.01	98.35	0.01	0.14	−37.8	–	−36.9	−127	1
	JT1	6852.5–7032.0	$Є_1c$	0.01	0.04	0.44	1.28	0.01	98.01	0.20	0.12	−38.4	−7.3	−36.98	−126	1
	JT1	6972	$Є_1c$	0.01	–	1.7	1.27	0.01	96.82	0.18	–	−38.2	−6.5	−36.4	−134	3
Nanchong block	CT1	6264	$Є_1c$	0.01	–	0.38	5	0.04	94.13	0.21	–	−35.8	1	−36.6	−136	3
DB1 block	DB1	6350.05	Z_2dn^4	0.00	0.58	29.20	0.13	0.00	69.80	0.27	0.00	−31.3	–	−31.3	−138	1
	DB1	6398	Z_2dn^4	0.01	0.02	0.46	26.45	2.05	70.92	0.07	29.35	–	–	–	–	1
	DB1	6297–6403.11	Z_2dn^4	0.02	0.01	0.33	12.86	2.34	84.39	0.05	33.53	–	–	–	–	1
	DB1	6537–6684	Z_2dn^4	0.04	0.04	0.52	17.96	11.8	69.6	0.04	169.28	−30.7	2.3	−26.3	−148	1
PS1 block	PS1	7232.5–7349.7	Z_2dn^4	0.08	0.11	0.97	48.52	2.46	47.83	0.03	35.27	−35.9	1.1	−29.1	−149	1
	PS1	7466.5–7680	Z_2dn^4	0.03	0.30	0.62	10.44	8.92	79.64	0.05	127.96	−32.8	−0.9	−27.8	−148	1
	PS1	7466.5–7680	Z_2dn^4	0.06	0.06	0.66	13.64	17.57	67.99	0.02	252.05	−34.4	−0.2	−28.8	−148	1
	PS1	7466.5–7680	Z_2dn^4	0.07	0.06	0.81	14.43	20.47	64.16	0.00	293.61	−34.5	−0.2	−28.8	−148	1
	PS5	5503–5588	Z_2dn^4	0.01	0.03	0.37	18.2	2.08	79.28	0.03	29.8	−33.0	–	−28.0	−151	1
JT1 block	PS7	7186–7243	Z_2dn^4	0.01	0.47	0.5	16.94	0.47	81.57	0.04	6.71	−32.2	0.7	−26.9	−134	1
	PS8	7009–7127	Z_2dn^4	0.01	0	0.19	9.09	0.55	90.14	0.02	7.86	−32	1.5	−26.2	−128	1
Zhongjiang block	ZJ2	6547	Z_2dn^2	0.05	–	0.67	15.43	6.8	76.9	0.04	–	−35.1	−1.5	−27.4	−141	3
	ZJ2	6547–6608	Z_2dn^2	0.02	0.06	0.53	15.05	4.99	79.33	0.01	71.56	−34.8	−1.3	−27.4	–	1
	ZJ2	6547–6608	Z_2dn^2	0.02	0.06	0.88	11.04	5.39	82.59	0.02	77.37	−34.8	−2.2	−27.3	–	1
	ZJ2	6693	Z_2dn^2	0.05	0.11	0.67	15.43	4.5	79.2	0.04	71.56	−35.1	–	−28.0	−141	1
	ZJ2	6804–6806	Z_2dn^2	0	0.14	93.08	0.19	–	6.57	0.02	–	−34.7	−19.4	−33.2	−133	1
	ZJ2	6804–6806	Z_2dn^2	0.02	0.04	93.04	0.24	0.00	6.64	0.02	0.00	−35.1	−16.4	−33.1	−131	1
PT1 block	PT1	5726–5817	Z_2dn^2	0.03	0.00	0.36	3.41	2.31	93.81	0.08	33.19	−33.6	−1.8	−28.9	−133	1
	PT1	5726–5817	Z_2dn^2	0.06	0.01	0.13	2.32	2.46	94.94	0.08	35.29	−33.9	−0.2	−29.2	−125	1
	PT1	5726–5817	Z_2dn^2	0.06	0.00	0.51	2.24	2.30	94.81	0.08	33.05	−34.0	−1.0	−29.2	−129	1
	PT1	5726–5817	Z_2dn^2	0.02	0.00	0.78	2.20	2.33	94.60	0.07	33.40	−33.9	−0.1	−29.3	−124	1
	PT1	5726–5817	Z_2dn^2	0.05	0.00	0.73	2.10	2.32	94.73	0.07	33.34	−33.9	−0.6	−29.2	−125	1
	PT1	5771	Z_2dn^2	0.01	–	0.56	4.42	2.11	92.83	0.07	–	−34.7	−0.2	−29.0	−140	1
	PT1	5771	Z_2dn^2	0.01	0.01	0.61	4.44	1.98	92.88	0.07	33.13	−34.3	–	−29.0	−140	3
	PT101	5615–5814	Z_2dn^2	0.02	0.00	0.40	3.40	2.40	93.69	0.09	34.38	−33.8	–	−28.9	−147	1
	PT101	5877	Z_2dn^2	0.01	–	0.55	5.88	2.52	90.96	0.07	–	−34.6	−4.3	−29.5	−141	4
	PT101	5990	Z_2dn^2	0.01	–	10.24	3.23	3.09	83.34	0.06	–	−34.7	−3.5	−29.0	−143	4
	PT102	5729–5864.89	Z_2dn^2	0.02	0.01	0.08	6.67	2.20	90.96	0.06	31.58	−34.0	–	−28.0	−144	1
	PT102	5905–5940	Z_2dn^2	0.04	0.12	0.14	6.14	3.02	90.46	0.08	43.35	−34.1	–	−28.8	−152	1
	PT102	5937	Z_2dn^2	0.02	–	0.8	5.25	3.71	89.88	0.06	–	−34.4	−0.3	−29.1	−137	4
	PT103	5725.0–5944.0	Z_2dn^2	0.03	0.01	0.42	7.01	2.58	89.91	0.04	37.04	−33.6	–	−27.1	−134	1
	PT103	5725.0–5944.0	Z_2dn^2	0.04	0.01	0.29	13.94	2.18	83.52	0.02	31.30	−33.6	–	−27.1	−148	1
	PT103	5759–5768	Z_2dn^2	0.38	0.2	31.85	0.26	0	67.25	0.05	0.00	−33.9	–	–	−149	1
	PT103	5782–5795.5	Z_2dn^2	0.35	0.15	66.00	0.60	0.00	32.81	0.09	0.00	−29.3	–	–	−144	1
	PT103	5807–5818	Z_2dn^2	0.23	0.29	59.42	0.27	0.00	39.74	0.05	0.00	−33.6	–	–	−154	1
	PT103	5844.5–5853	Z_2dn^2	0.18	0.27	49.74	0.21	0	49.57	0.03	0.00	−33.6	–	–	−154	1
	PT103	5924.5–5928	Z_2dn^2	0.10	0.08	11.64	0.07	–	88.04	0.07	–	−33.1	–	–	−146	1
	PT108	5871–5913	Z_2dn^2	0.01	0.05	0.5	4.2	2.1	93.13	0.01	30.13	−33.0	–	−24.7	−141	1
	PT109	5851–6040	Z_2dn^2	0.01	0.16	0.68	15.35	1.71	82.06	0.03	24.55	−34.1	1.0	–	−141	1

Note: 1 = This study, 2= Xie et al., 2020 3 = Xie et al., 2021a, 4 = Wei et al., 2022.

lower. P_2m hydrocarbon gases are characterized by increased CH_4 (85.34 % to 97.14 %) and C_2H_6 (0.23 % to 0.4 %) content. Notably, P_2m natural gas from wells NC1, NC3, and ZJ1 more closely resembles the hydrocarbon gas composition of the $Є_1l$, $Є_1c$, and $Є_3x$ (Fig. 2a).

4.1.2. Non-hydrocarbon gas composition

In the Penglai gas area, the Sinian–Permian multiple strata natural gas accumulation is characterized by a significant presence of non-hydrocarbon gases, primarily dominated by N_2, He, CO_2, and H_2S. Notably, the Sinian Z_2dn^2 and Z_2dn^4 exhibit the highest content of non-hydrocarbons, which correlates with a reduced CH_4 content (Fig. 2a, 3, Table. 1).

The distribution of N_2 across the Sinian-Permian gas accumulation in the Penglai gas area is broad, ranging from 0.07 % to 93.04 %, with most samples ranging between 0.07 % and 0.97 %. This contrasts with the Permian P_2m, where N_2 levels are uniformly lower, ranging from 0.13 % to 0.24 % (Fig. 3a). The N_2 content in Z_2dn from specific wells, such as ZJ2 and PT103, deviates significantly, reaching up to 93.04 % and 66 %, respectively. These wells are located near strike-slip faults on the platform margin of the Z_2dn^2, with the upper part of Z_2dn^2 in contact with high-maturity source rocks. N_2 in the central Sichuan basin originates from organic matter in source rocks through thermal maturation or deep magmatic processes (Qin et al., 2024; Zhao et al., 2021).

The threshold for commercial helium content in natural gas is 0.1 % (Zhang et al., 2023b). In Z_2dn, He content varies from 0.01 % to 0.38 %, suggesting a relatively high concentration with potential for exploitation. In contrast, the Cambrian gas accumulation has an average helium content of 0.01 %, with overall low levels (0.01 %–0.02 %), lacking commercial value. The He content in P_2m ranges from 0.01 % to 0.03 %, slightly higher than that of the Cambrian, yet still below the industrial threshold (Fig. 3a).

H_2S in Sinian-Permian gas accumulation primarily results from TSR (Liu et al., 2022a; Liu et al., 2016; Zhang et al., 2024; Zhu et al., 2021). H_2S content is a good indicator of the TSR reaction intensity, with higher levels usually suggesting a more vigorous reaction. The Sinian Z_2dn^2 and Z_2dn^4 exhibit significantly higher H_2S contents (0.4 %–21.78 %) (Fig. 3b), whereas the Cambrian $Є_1l$, $Є_1c$, $Є_3x$, and P_2m have lower levels (0.36 %–0.01 %) (Fig. 3b). CO_2 is also a by-product of the TSR reaction. However, CO_2 content exceeding 8 % and a $\delta^{13}C_{CO2}$ value greater than −10 ‰ is predominantly of inorganic origin, often associated with acidizing operations (Xie et al., 2021b). Excluding these high CO_2 instances, the highest CO_2 content is observed in Z_2dn^2.

4.2. Stable isotope composition of natural gases

4.2.1. Carbon isotope characteristics of natural gas

The $\delta^{13}C_{CH_4}$ and $\delta^{13}C_{C_2H_6}$ values of the natural gas of the Sinian-Permian multi-strata in the Penglai gas area exhibit a broad range: from −38.7 ‰ to −27.7 ‰ for $\delta^{13}C_{CH_4}$ and from −39.6 ‰ to −23.4 ‰ for $\delta^{13}C_{C_2H_6}$ (Fig. 4a). Generally, the isotope values of natural gases from different Sinian-Permian strata differ.

(1) Natural gases from Cambrian $Є_1c$, $Є_1l$, and $Є_3x$ are characterized by relative lower $\delta^{13}C_{CH_4}$ (−38.7 ‰ – −35.8 ‰) and lower $\delta^{13}C_{C_2H_6}$ (−39.6 ‰ – −36.4 ‰), with a reversed carbon isotope order ($\delta^{13}C_{CH_4}$ greater than $\delta^{13}C_{C_2H_6}$).
(2) Natural gas from P_2m featuring relative greater $\delta^{13}C_{CH_4}$ (−35 ‰ – −27.7 ‰) and $\delta^{13}C_{C_2H_6}$ (−35.4 ‰ – −30 ‰). In these gases, the carbon isotope order is mostly reversed, with $\delta^{13}C_{CH_4}$ being greater than $\delta^{13}C_{C_2H_6}$.
(3) Sinian natural gases from the Z_2dn^2 and Z_2dn^4 have greater $\delta^{13}C_{CH_4}$ (−35.1 ‰ – −29.4 ‰) and greater $\delta^{13}C_{C_2H_6}$ (−29.8 ‰ – −23.4 ‰) values. The carbon isotope order in these gases is predominantly in a positive sequence, with $\delta^{13}C_{CH_4}$ less than $\delta^{13}C_{C_2H_6}$.

We employed unsupervised machine learning, specifically clustering analysis, and categorized natural gas into three groups based on $\delta^{13}C_{CH_4}$ and $\delta^{13}C_{C_2H_6}$ isotopes.

(1) The first cluster includes natural gas from $Є_1c$, $Є_1l$, and $Є_3x$, along with some samples from Z_2dn^2 and Z_2dn^4, characterized by marginally lower $\delta^{13}C_{CH_4}$ and $\delta^{13}C_{C_2H_6}$ values.
(2) The second cluster consists of P_2m natural gas, as well as some samples from Z_2dn^2 and Z_2dn^4, distinguished by elevated $\delta^{13}C_{CH_4}$ levels.
(3) The third cluster remains exclusively natural gas from Z_2dn^2 and Z_2dn^4.

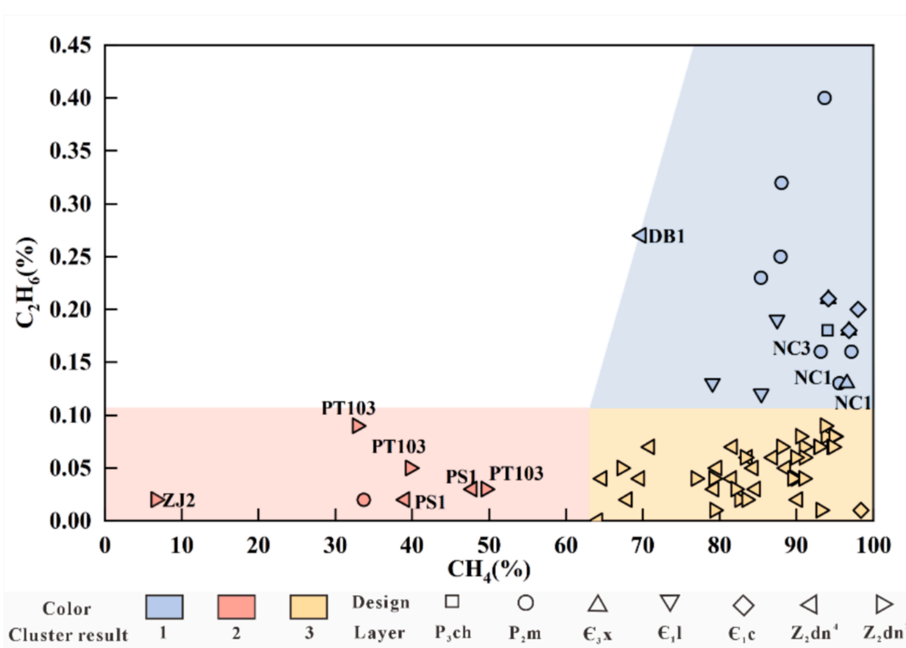

Fig. 2. Relationship between hydrocarbon composition of CH_4 – C_2H_6 of Sinian – Permian system in Penglai gas area (data sources are listed in Table 1).

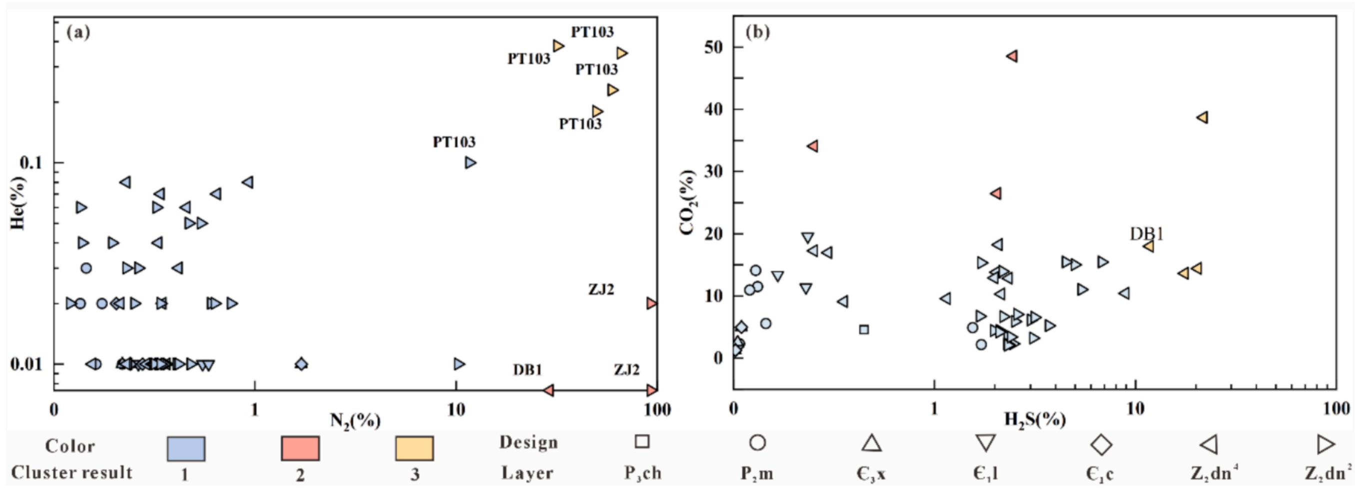

Fig. 3. Relationship between different non-hydrocarbon composition of Sinian – Permian system in Penglai gas area. (a) He vs N_2; (b) CO_2 vs H_2S. (data sources are listed in Table 1).

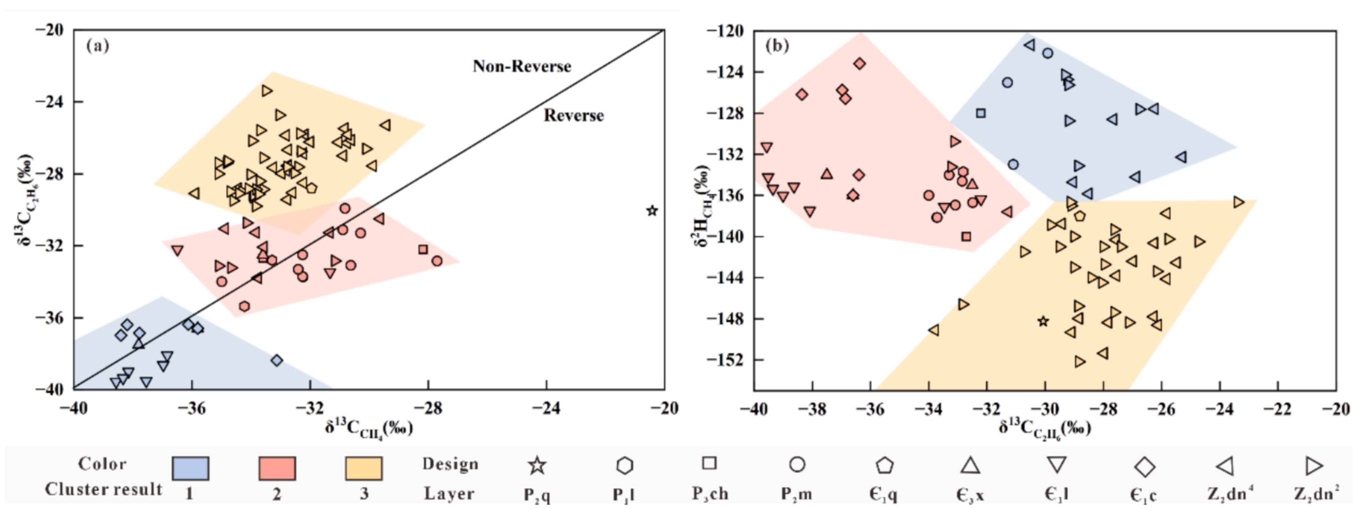

Fig. 4. Relationship between carbon and hydrogen isotopic of Sinian – Permian system in Penglai gas area. (a) $\delta^{13}C_{CH_4}$ vs $\delta^{13}C_{C_2H_6}$; (b) $\delta^2H_{CH_4}$ vs $\delta^{13}C_{C_2H_6}$. (data sources are listed in Table 1).

4.2.2. Hydrogen isotope characteristics of natural gas

The $\delta^2H_{CH_4}$ of natural gases from the Sinian-Permian multi-strata within the Penglai gas area varies widely, from −156.7 ‰ to −121.4 ‰, with overlapping ranges across different layers. The $\delta^2H_{CH_4}$ of P_2m, Є$_1$l, and Є$_3$x natural gases are closely aligned, with relatively higher overall values ranging from −140 ‰ to −123 ‰. Notably, the $\delta^2H_{CH_4}$ of Є$_1$c natural gas is marginally higher than that of P_2m (Fig. 4b). In contrast, the $\delta^2H_{CH_4}$ of Z_2dn^2 and Z_2dn^4 natural gas spans from −157 ‰ to −128 ‰, slightly lower than the values observed in the Permian and Cambrian natural gases (Fig. 4b).

4.3. Reservoir characteristics

4.3.1. Petrographic characteristics

Core and microscopic observations reveal that Z_2dn of the Penglai gas area exhibits distinct hydrothermal alteration characteristics. These features include the presence of saddle dolomite around the margin of dissolution pores and cavities (Fig. 5a, b, c, d). Saddle dolomite, is widely recognized as an indicator of hydrothermal activity (Jiang et al., 2017) and exhibits luminescence under cathode ray illumination (Fig. 5c). The original fine-grained micritic dolomite has transformed into coarser crystalline dolomite through recrystallization, attributed to the effects of deep hydrothermal fluids (Fig. 5c). This transformation often results in secondary enlargement of dolomite crystals along their margins.

As deep hydrothermal fluids ascend along basement faults and experience a temperature reduction, they promote the formation of minerals like sphalerite and galena, which can be incorporated into the dolomite or occupy dissolution cavities created by the fluids. Accompanying galena (Fig. 5e) and sphalerite (Fig. 5f, g and h), other hydrothermal accessory minerals such as pyrite (Fig. 5g), quartz, and fluorspar (Fig. 5i) also form. These minerals are often associated with saddle dolomite within dissolution pores. The widespread presence of metal sulfides like galena, sphalerite, and pyrite suggests that the hydrothermal fluids contain significant sulfur, notable even without extensive gypsum-salt layers in the neighbouring strata. The sulfur could potentially act as a source for the TSR reaction.

4.3.2. Isotopic characteristics

In the Penglai gas area, the $\delta^{18}O$ and $\delta^{13}C$ values of Z_2dn dolomite differ distinctly from those of the late Proterozoic paleo-seawater (Fig. 6a). The $\delta^{18}O$ values of Z_2dn dolomite range from −7.3 ‰ to −3 ‰, and the $\delta^{13}C$ values range from 0.6 ‰ to 3.8 ‰, whereas late Proterozoic paleo-seawater has $\delta^{18}O$ values of −0.5 ‰ to 1.5 ‰ and $\delta^{13}C$

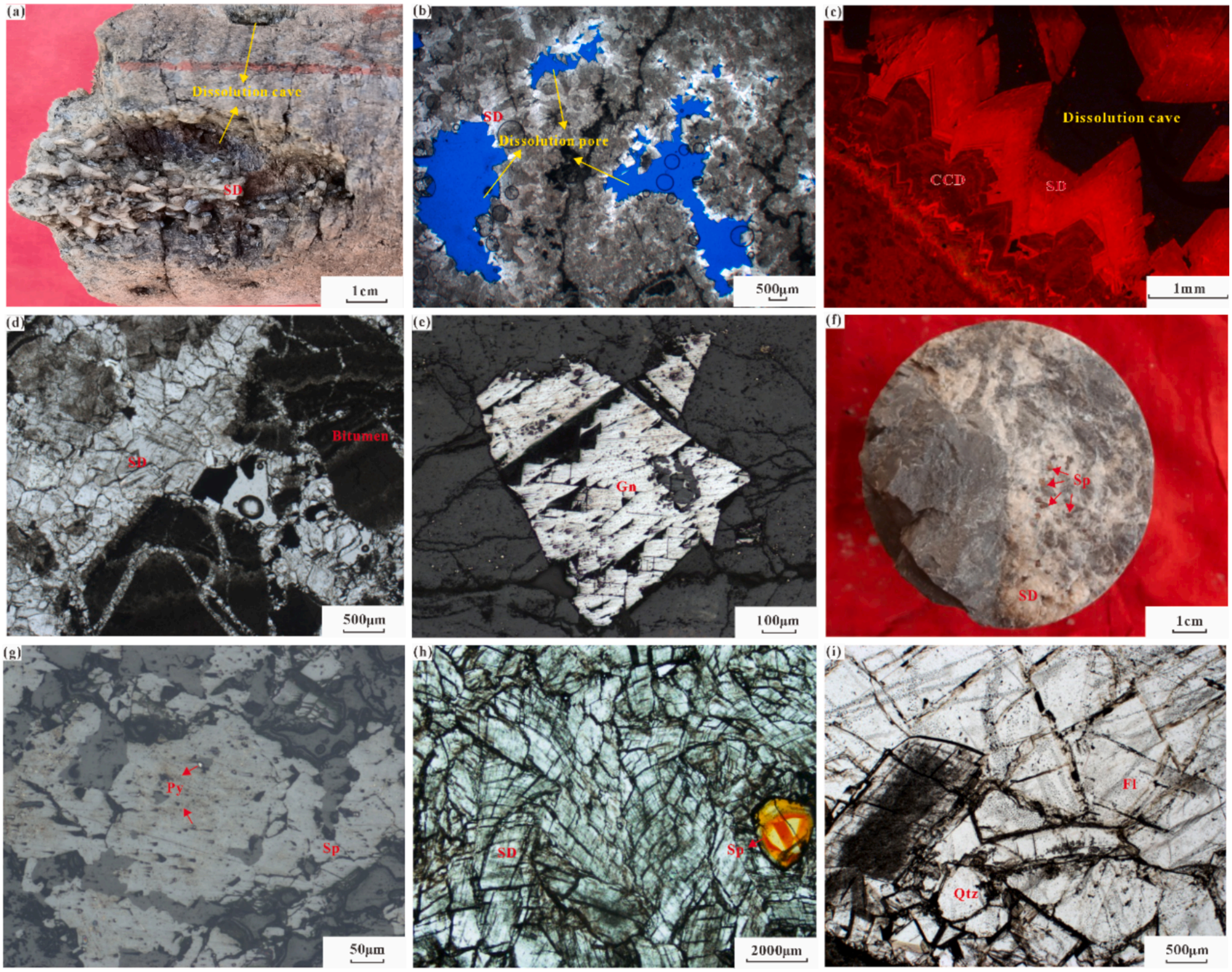

Fig. 5. Core and microscopic observation characteristics of Z_2dn in the Penglai gas area Figs b, c, d, e, g, h, i supplied by Research Institute of Petroleum Exploration & Development in PetroChina Southwest Oil & Gas Oilfield Company. (a) PS3, Z_2dn^2, 5769.51 m – 5769.58 m, algal sandy debris dolomite, cave development, saddle dolomite(SD) and bitumen are seen in the dissolution cave, core photo; (b) PT101, Z_2dn^2, 5737.09 m, algal laminated dolomite, dissolution pore development, and the edge of the development of saddle dolomite, polarized light Microphotographs; (c) PT102, 5867.72 m, Z_2dn^2, mud crystal dolomite, the edges of dissolution pore development of coarse crystalline dolomite in turn(CCD) and saddle dolomite, saddle dolomite glows under cathode rays, cathodoluminescence (CL) photo; (d) PT1, Z_2dn^2, 5747.29 m – 5747.37 m, pores are filled by saddle dolomite and bitumen, polarized light Microphotographs; (e) PT1, Z_2dn^2, 5747.29 m – 5747.37 m, galena (Gn) development, polarized light Microphotographs; (f) PS4, Z_2dn^2, 6221.98 m,is powder crystal dolomite, with prevalent saddle dolomite and sphalerite(Sp), core photo; (g) PT1, Z_2dn^2, 5727 m. development of pyrite(Py), sphalerite, polarized light Microphotographs; (h) PS4, Z_2dn^2, 6220.97 m, powder crystal dolomite, development of saddle dolomite, with sphalerite development, polarized light Microphotographs; (i) PT102, Z_2dn^2, 5870.75 m, mud crystal dolomite, development of quartz(Qtz), fluorspar(Fl), polarized light Microphotographs.

values of 4 ‰ to 6 ‰ (Fairchild and Spiro, 1987; Zempolich et al., 1988). Both the $\delta^{18}O$ and $\delta^{13}C$ values of Z_2dn dolomite are lower than those of the paleo-seawater (Fig. 6a).

The $^{87}Sr/^{86}Sr$ ratios of Z_2dn dolomite in the Penglai gas area range from 0.708881 to 0.710170, whereas the $^{87}Sr/^{86}Sr$ ratio of the paleo-seawater during the deposition of Z_2dn is approximately 0.7085 (Jiedong et al., 1999). Therefore, the $^{87}Sr/^{86}Sr$ ratios of Z_2dn dolomite are higher than those of the paleo-seawater during the deposition period (Fig. 6b).

4.3.3. Fluid inclusions

Microscopic observation of inclusions and laser Raman spectroscopy revealed various inclusion types within hydrothermal minerals, including quartz and ankerite, in the dolomite reservoir of the Penglai gas area.

(1) Gas-phase inclusions: These inclusions contain CH_4 and non-hydrocarbon gases like H_2S and CO_2 (Fig. 7a, b). Under high-temperature conditions (100–140 °C or more), petroleum hydrocarbons undergo thermochemical sulfate reduction (TSR), yielding H_2S, CO_2, and other acid gases. As the reaction progresses, gaseous hydrocarbons such as C_2H_6 also participate, resulting in gases primarily composed of CH_4, and non-hydrocarbon gases (H_2S, CO_2).
(2) Liquid-phase inclusions: Characterized by black cylindrical shapes, these inclusions are predominantly composed of solid bitumen (Fig. 7c). During the early stages of TSR, high-molecular-weight liquid hydrocarbons are primarily involved, with solid bitumen as a key product of the reaction (Liu et al., 2022a).
(3) Gas-liquid two-phase inclusions: These inclusions contain gaseous hydrocarbons, including CH_4, and solid bitumen (Fig. 7d). The coexistence of bitumen and CH_4 indicates that

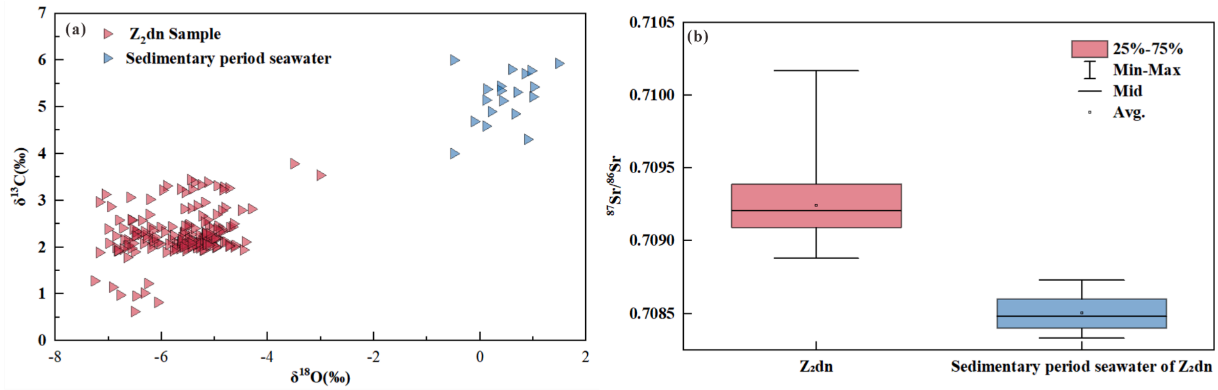

Fig. 6. Distribution of carbon and oxygen isotopes (a) and strontium isotopes (b) in Z_2dn of the ZJ 2 well in the Penglai gas area.

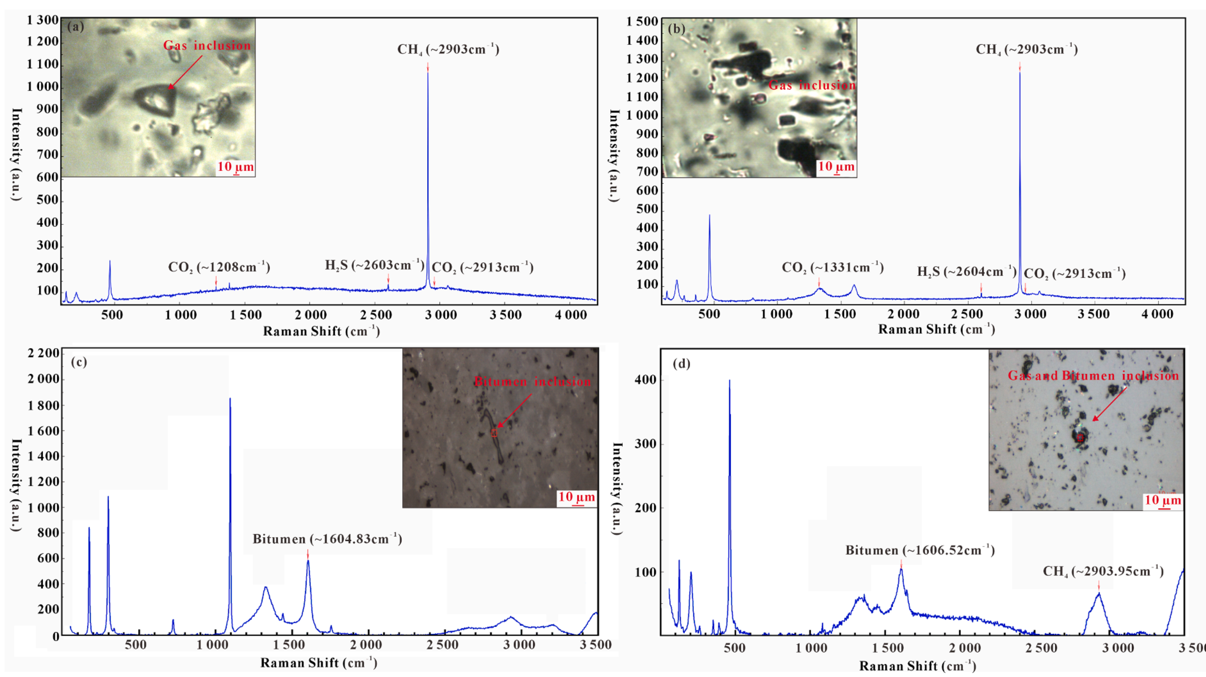

Fig. 7. Characteristics of fluid inclusions and laser Raman spectra of Z_2dn in the Penglai gas area. (a) PT1, Z_2dn, gas-phase inclusions in quartz with CO_2, H_2S, CH_4; (b) PT1, Z_2dn, gas-phase inclusions in dolomite with CO_2, H_2S, CH_4; (c) PS2, Z_2dn, 7782.24 m, liquid-phase inclusions in ankerite, cylindrical, with darker walls and bitumen as the main composition; (d) PT102, Z_2dn, 5865.44 m – 5865.5 m, gas–liquid two-phase inclusions in dolomite, mostly black in color, with alkanes as the main composition and a small amount of bitumen.

high-molecular-weight hydrocarbons were initially present in the fluid inclusions and likely underwent cracking or were affected by TSR in later stages.

5. Discussion

5.1. Hydrothermal activity and TSR evidence

As mentioned, hydrothermal mineral assemblages and inclusions containing H_2S indicate that the Z_2dn natural gas is influenced by TSR induced by hydrothermal fluids. The stable isotope composition of carbon ($\delta^{13}C$) and oxygen ($\delta^{18}O$) in dolomite is essential for understanding its genesis and provides insights into the dolomitization fluids. These isotopic signatures are influenced by the salinity and temperature of the paleo-seawater during the diagenetic processes that formed the dolomite. The $\delta^{18}O$ and $\delta^{13}C$ values of seawater serve as a baseline for interpreting the $\delta^{18}O$ and $\delta^{13}C$ values of dolomite. Given the variability of seawater's stable isotope values throughout geological history, researchers have contextualized their findings by relying on estimates of $\delta^{18}O$ and $\delta^{13}C$ for Late Proterozoic seawater. Fairchild and Spiro (1987) and Zempolich et al. (1988) estimated Late Proterozoic seawater $\delta^{13}C$ values range from 5 ‰ to 7 ‰ and $\delta^{18}O$ values from −0.5 ‰ to 0.9 ‰. Yang et al. (1999) studied $\delta^{18}O$ and $\delta^{13}C$ data from carbonate rocks of the Sinian Doushantuo Formation in the Yangtze region, suggesting Sinian seawater had $\delta^{13}C$ values less than 4 ‰ to 6 ‰ and $\delta^{18}O$ values of −0.5 ‰. By comparing the $\delta^{18}O$ and $\delta^{13}C$ values of dolomite with estimated values of paleo-seawater, researchers can make preliminary inferences about the conditions under which the dolomite formed, including the potential sources of dolomitization fluids and the diagenetic environment.

The $\delta^{18}O$ and $\delta^{13}C$ values of dolomite from the Z_2dn in the Penglai gas area exhibit significant deviations from those of Late Proterozoic seawater (Fig. 6a). The $\delta^{18}O$ values for Z_2dn dolomite range from −7.269 ‰ to −3.021 ‰, and the $\delta^{13}C$ values from 0.624 ‰ to 3.785 ‰, both lower than the estimated values for Late Proterozoic seawater. These lower $\delta^{18}O$ values suggest that the dolomite formed at higher temperatures, as higher diagenetic temperatures typically result in lower $\delta^{18}O$ in carbonate minerals (Han et al., 2019). Additionally, thermal isotope fractionation may have occurred, with greater ^{18}O preferentially entering the fluid phase and lower ^{16}O being incorporated into the dolomite, leading to lower $\delta^{18}O$ values in hydrothermally influenced dolomite (Jiang, 2015). The lower $\delta^{13}C$ values could be due to oxidation of organic matter, which produces CO_2 with a lower $\delta^{13}C$, affecting the $\delta^{13}C$ of the carbonate minerals (Swart, 2015). These isotopic signatures indicate a diagenetic environment influenced by hydrothermal activity and possibly organic matter oxidation.

Strontium isotopes, specifically the $^{87}Sr/^{86}Sr$ ratio, indicate the origin of carbonate minerals and diagenetic fluids (Banner, 1995). The $^{87}Sr/^{86}Sr$ of seawater reflects paleo-seawater and is predominantly influenced by crustal and mantle sources, with significant changes occurring primarily during global tectonic events. Consequently, seawater's $^{87}Sr/^{86}Sr$ ratio can be assumed stable over geological timescales. Our study adopted the $^{87}Sr/^{86}Sr$ value(average 0.7085) from (Yang et al., 1999) as representative of the paleo-seawater during the deposition of Z_2dn (Fig. 6b). Silica-aluminate-rich granite is abundant in ^{87}Rb, a radioactive isotope decays through beta decay to form the stable isotope ^{87}Sr. When deep hydrothermal fluids interact with silica-aluminate-rich granite, they incorporate ^{87}Sr of radioactive origin, leading to higher $^{87}Sr/^{86}Sr$ ratios in the resulting Z_2dn dolomite compared to the depositional paleo-seawater.

5.2. Factors controlling the differences in natural gas composition

5.2.1. Maturity – hydrocarbon gas composition

The composition of hydrocarbon gases is influenced by maturity. As maturity increases, the content of CH_4 rises, while heavier hydrocarbons like C_2H_6 decline, and the dryness factor progressively increases (Xie et al., 2021a). This trend is evident in the Penglai gas area, where the maturity of Sinian-Permian natural gas is notably high. The hydrocarbon gases predominantly consist of CH_4, with minimal C_2H_6 content (0.09 %–0.01 %) (Table 1) and a high dryness (>0.996). Notably, Z_2dn natural gas exhibits the highest dryness (0.998–1.0), corresponding to the highest maturity and CH_4 content. In contrast, the P_2m gas has the lowest dryness (0.996–0.998), lowest maturity, and highest C_2H_6 content (0.15 %–0.40 %). The maturity of Cambrian natural gas ($Є_1$c, $Є_1$l, and $Є_3$x) falls between those of the Sinian and Permian. A three-cluster solution was identified by applying hierarchical clustering to the hydrocarbon composition data of CH_4 and C_2H_6(Fig. 2a). The first cluster comprises natural gas from the Z_2dn^2, Z_2dn^4 and P_2m (PT101 well), characterized by relatively low CH_4 and C_2H_6 levels, attributed to a high proportion of non-hydrocarbon gases. The second cluster includes natural gas from the Z_2dn^2 and Z_2dn^4 with relatively low C_2H_6 and high CH_4 content, as well as gas from $Є_1$l, and $Є_3$x with varying C_2H_6 levels due to higher maturity. The third cluster primarily comprises natural gas from P_2m, featuring high CH_4 and C_2H_6 content, with a few samples from $Є_1$l, $Є_1$c, and $Є_3$x exhibiting high C_2H_6 content due to lower maturity (Fig. 2a).

5.2.2. Deep inorganic gas sources – non-hydrocarbon gas composition

Among non-hydrocarbon gases, He and N_2 are closely associated with deep-seated interactions. In the Z_2dn gas, there is a positive correlation between He and N_2 content (Fig. 3a), with nitrogen enhancing helium's enrichment (Cheng et al., 2023; Qin et al., 2024; Wang et al., 2023). In contrast, unlike N_2, hydrocarbon gases, CO_2, and H_2S tend to dilute helium content (Table 1). This suggests that the presence of N_2 is conducive to helium accumulation, while other gases may act as diluents, affecting the overall concentration of helium in the gas mixture.

Helium in natural gas primarily originates from atmospheric, crustal, and mantle sources, with crustal and mantle sources predominant (Liu et al., 2022b; Zhang et al., 2023b). Crustal-sourced helium (Peng et al., 2022), specifically ^4He (You et al., 2023), is primarily produced by radioactive decay of uranium (^{235}U and ^{238}U) and thorium (^{232}Th). Good helium sources generally include basement rocks and hydrocarbon source rocks with high maturity and radioactivity. In the central Sichuan Basin, helium predominantly originates from the decay of U and Th in crustal sources such as mature source rocks and deep granitic rocks (Wei et al., 2014a; Zhang et al., 2023c).

Nitrogen has three origins: released by the organic or inorganic matter of sediments, inorganic nitrogen sourced from the crust or mantle, and the paleo-atmosphere. The $\delta^{15}N$ values of N_2 of Sinian-Permian multi-strata in the central Sichuan Basin range from −8 ‰ to −3 ‰ (Zhao et al., 2021). These isotopic values suggest a significant contribution from thermally altered organic matter in the source rocks. Additionally, the proximity of exploration wells to strike-slip faults implies a potential connection to deep magmatic nitrogen sources (Fu et al., 2023; Qin et al., 2024; Zhao et al., 2021). The dual influence of organic and magmatic sources provides insights into the complex nitrogen cycling and migration processes.

The observed pattern of low He content in the Cambrian and high He content in the Sinian and Permian (Fig. 3a) is linked to the deep granite source and the varying strata penetrated by strike-slip faults. Helium and nitrogen source rocks are predominantly deep granites beneath Sinian. The enrichment of He and N_2 in natural gas accumulations largely depends on these faults' connectivity with gas-bearing formations. When strike-slip faults extend from the basement only to the Z_2dn, He and N_2 are enriched solely in Z_2dn. In contrast, if faults reach the P_2m, upward migration of gas or fluids from granites leads to He and N_2 accumulation at the base and top. The middle strata will be more susceptible to more pronounced faulting, resulting in poorer preservation conditions and causing natural gas to migrate upwards, with minimal intermediate strata enrichment. This migration pattern explains the low He content in Cambrian natural gas and the high He and N_2 content in Sinian and Permian natural gas. Additionally, the high non-hydrocarbon gas content in the Z_2dn also diminishes hydrocarbon content. N_2 can also be produced by high-maturity $Є_1$q source rock through thermal maturation (Wei et al., 2014b). This process contributes to the enrichment of N_2 in Cambrian non-hydrocarbon gas, albeit with relatively low He content. This complex interplay of geological structures, source rock maturity, and fault connectivity determines the distribution and concentration of gases in these formations.

A three-cluster solution was identified by applying hierarchical clustering to the non-hydrocarbon composition data of He and N_2(Fig. 3a). Firstly, one cluster is the Z_2dn gas samples from the PT103 well with high He and high N_2 content. Due to the good positive correlation between He and N_2, it may be related to the influence of Crustal-sourced inorganic gas; Secondly, Another cluster is the Z_2dn gas samples from ZJ2 and DB1 wells with high N_2 and low He content, which may be due to the influence of thermally altered organic matter of source rocks leading to high N_2 content; The last cluster natural gas exhibits low He and low N_2 content from the remaining Z_2dn, Є and P_2m, which are less affected by inorganic gas.

5.2.3. Hydrothermal and TSR reactions – acidity

Petrographic observations reveal significant occurrences of saddle dolomites and metal sulfides coupled with H_2S and CO_2 in fluid inclusions, indicating that the Sinian Z_2dn^2 and Z_2dn^4 underwent TSR. This process not only alters the mineral composition but also significantly impacts gas composition. Among non-hydrocarbon gases, the levels of H_2S and CO_2 in Sinian Z_2dn^2 and Z_2dn^4 natural gas accumulations are notably higher than in Cambrian and Permian (Fig. 3b). Given that H_2S is a primary product of TSR, while CO_2 is a by-product, the elevated levels of these gases strongly suggest TSR's influence on altering the natural gas composition.

Similarly, to illustrate the effect of TSR on natural gas composition, hierarchical clustering was used to group the samples by combining H_2S and CO_2 content. Since acidizing operations affect CO_2 content, it is not possible to effectively distinguish natural gas based on H_2S and CO_2 content (Fig. 3, b).

5.3. Mechanisms of carbon and hydrogen isotope differences in natural gas

The $\delta^{13}C_{C_2H_6}$ of natural gas typically reflects its source rock, serving as a key indicator for distinguishing between oil-type and coal-type gases, with a threshold around −28 ‰ to −29 ‰ for effective genesis identification in conventional settings (Dai, 1993). However, this criterion is not universally applicable, particularly in (ultra-) deep and high-maturity contexts like the Penglai gas area. For instance, the Z_2dn^2 and Z_2dn^4 gases exhibit $\delta^{13}C_{C_2H_6}$ values consistently greater than −28 ‰, reaching up to −23.4 ‰ (Fig. 4a), suggesting a coal-type origin. Nevertheless, the overlying and underlying Є$_1$q and Z_2dn^3 source rocks are dominated by sapropelic organic matter (Fu et al., 2022; Wei et al., 2015). Consequently, the greater $\delta^{13}C_{C_2H_6}$ values in Z_2dn^2 and Z_2dn^4 gases cannot be attributed to humic organic matter.

Given the influence of multiple factors on $\delta^{13}C_{C_2H_6}$, it is not the sole criterion for classifying natural gas genesis. Instead, a combination of $\delta^{13}C_{CH_4}$ and hydrocarbon composition content is employed to determine the origin. In the Penglai gas area, the Sinian-Permian natural gas is thermogenic, predominantly derived from oil cracking, with the organic matter primarily being type II kerogen. The P_2m natural gas shows signs of influence from humic organic matter, leaning towards type III kerogen (Fig. 8a). Due to high maturity, most natural gas samples lack propane, with a vitrinite reflectance (R_o) exceeding 2.0 %. These results support those of previous studies. (Fig. 8b).

5.3.1. Differences in source rocks

Hydrocarbons retain isotopic signatures throughout their thermal evolution. Isotopic fractionation kinetics dictate that as kerogen cracks into crude oil, the carbon isotope value of generated oil is typically 1 ‰ to 3 ‰ lower than that of kerogen (Liu et al., 2010). As oil further cracks into solid bitumen and natural gas, the carbon isotope value of solid bitumen increases by approximately 2 ‰ to 3 ‰ (Liu et al., 2012), while the value for natural gas is slightly lower than that of solid bitumen by about 2 ‰ to 5 ‰ (Lei et al., 2018; Liu et al., 2010; Shuai et al., 2021). Thus, the genesis of natural gas can be ascertained from its carbon isotopic composition, providing insights into its evolutionary history.

The carbon isotope $\delta^{13}C$ characteristics of natural gas from the Cambrian Є$_1$c, Є$_1$l, and Є$_3$x are similar (Figs. 4 and 9), with values generally lower than those of Cambrian reservoir bitumen (−36.6 ‰ to −32 ‰). The $\delta^{13}C$ of solid bitumen closely aligns with that of the Є$_1$q source rock (kerogen's $\delta^{13}C$, −36.8 ‰ to −30 ‰), consistent with isotope fractionation kinetics and indicating a strong genetic relationship. Since Є$_1$c directly overlays the Є$_1$q source rock, it is inferred that the natural gases of Є$_1$c, Є$_1$l, and Є$_3$x originate from the Є$_1$q source rock, displaying characteristics of oil-cracked gas. Notably, the $\delta^{13}C_{CH_4}$ and $\delta^{13}C_{C_2H_6}$ values of Є$_3$x natural gas from the NC1 well are significantly greater than those of other Cambrian gases in the Penglai gas area and are similar to P_2m natural gas from other wells (Fig. 9), suggesting a probable contribution from the P_2m source rocks.

The $\delta^{13}C_{CH_4}$ and $\delta^{13}C_{C_2H_6}$ values of natural gas from Z_2dn^2 and Z_2dn^4 are greater than the $\delta^{13}C$ of reservoir solid bitumen (−38.2 ‰ to −33.6 ‰). This difference is attributed to an intense TSR reaction impacting Z_2dn^2 and Z_2dn^4 natural gas. TSR has a marginal effect on $\delta^{13}C_{CH_4}$, while significantly increasing the $\delta^{13}C_{C_2H_6}$. During this process, H_2S preferentially reacts with C_2H_6 resulting in ^{13}C-enriched residual ethane while producing ^{13}C-depleted ethanethiol (Cai et al., 2003; Zhang, 2019; Zhang et al., 2008). Ethanethiol then undergoes aromatic condensation and polymerization, incorporating into bitumen and making bitumen more depleted in ^{13}C. As more ^{12}C-enriched C_2H_6 is consumed, the remaining C_2H_6 becomes relatively enriched in ^{13}C, leading to a $\delta^{13}C_{C_2H_6}$ greater than $\delta^{13}C$ of bitumen (Zhang, 2019; Zhu et al., 2021). This results in the $\delta^{13}C$ of bitumen being 5 ‰ to 7 ‰ lower compared to non-TSR-affected bitumen (Machel et al., 1995). Consequently, the $\delta^{13}C$ of reservoir solid bitumen in Z_2dn^2 and Z_2dn^4 is lower than the $\delta^{13}C_{CH_4}$ and $\delta^{13}C_{C_2H_6}$. The $\delta^{13}C_{CH_4}$ values of Z_2dn^2 and Z_2dn^4 natural gas are

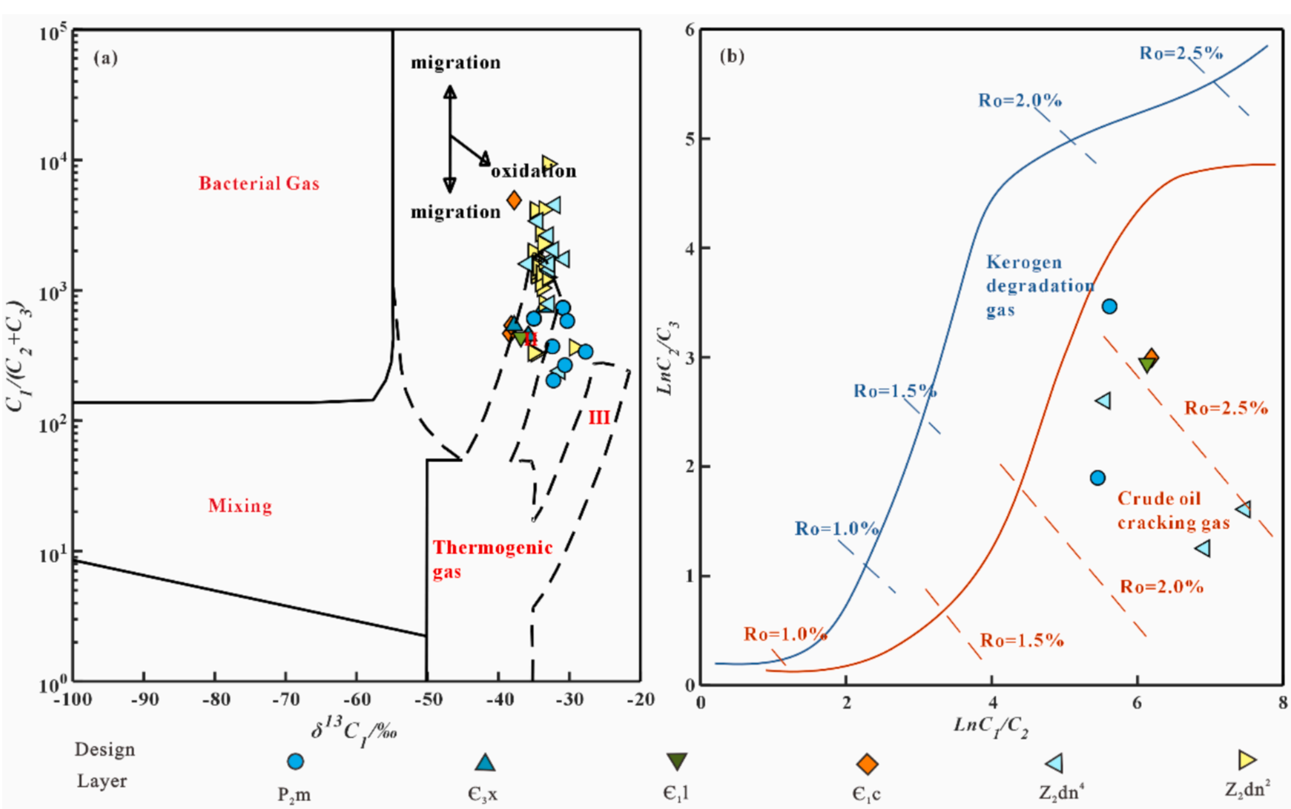

Fig. 8. Genetic type diagram of natural gas of Sinian – Permian system in Penglai gas area. (a)Modified from (Whiticar, 1994, 1999); (b) Modified from (Xie et al., 2016); (data sources are listed in Table 1);

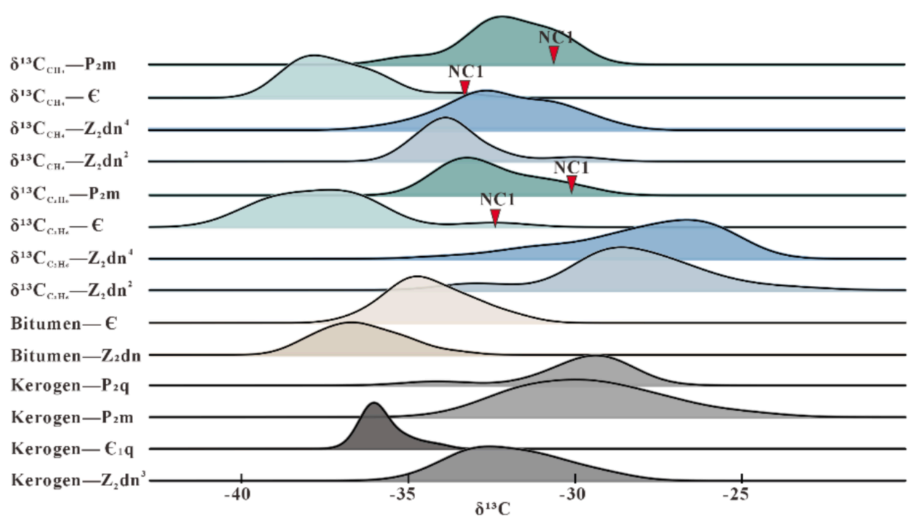

Fig. 9. Carbon Isotope Distribution of Natural Gas, Bitumen and Kerogen of Sinian-Permian system in Penglai gas area (data sources are listed in Table 1).

comparable to the $\delta^{13}C$ of Є1q kerogen (−36.8 ‰ to −30 ‰) and Z_2dn^3 source rock kerogen (−34.5 ‰ to −29 ‰) (Fig. 9), suggesting that Z_2dn^2 and Z_2dn^4 natural gas originates from Є1q and Z_2dn^3 source rocks.

The $\delta^{13}C_{CH_4}$ values of the P_2m natural gas closely resemble those of the Z_2dn^2 and Z_2dn^4 gases (Fig. 9), suggesting a common origin from the Є1q source rock. However, the kerogen $\delta^{13}C$ values of the P_2m-P_2q source rock (–33 ‰ to −25.1 ‰) are slightly greater than the Z_2dn^3 source rock's kerogen $\delta^{13}C$ values (−34.5 ‰ to −29 ‰). Additionally, the source of P_2m natural gas exhibits characteristics of type III kerogen, indicating a partial contribution from P_2m-P_2q source rocks. Conversely, the $\delta^{13}C_{C_2H_6}$ values of P_2m natural gas are lower than those of Z_2dn^2 and Z_2dn^4, suggesting that the P_2m natural gas has undergone less modification. The greater $\delta^{13}C_{CH_4}$ and $\delta^{13}C_{C_2H_6}$ values in the P_2m gas from NC1 well are primarily attributed to the influence of the P_2m-P_2q source rocks of the Middle Permian, yet the contribution from the Є1q source cannot be entirely discounted.

5.3.2. *Maturity differences and fractionation effects*

The wetness ratio (C_2^+/C_1^+) effectively mirrors changes in natural gas maturity (Xie et al., 2021a), with maturity increasing as C_2^+/C_1^+ decreases. In the Sinian-Cambrian gas, there is a strong correlation between C_2^+/C_1^+ and $\delta^{13}C_{CH_4}$, influenced by maturity (Fig. 10a).

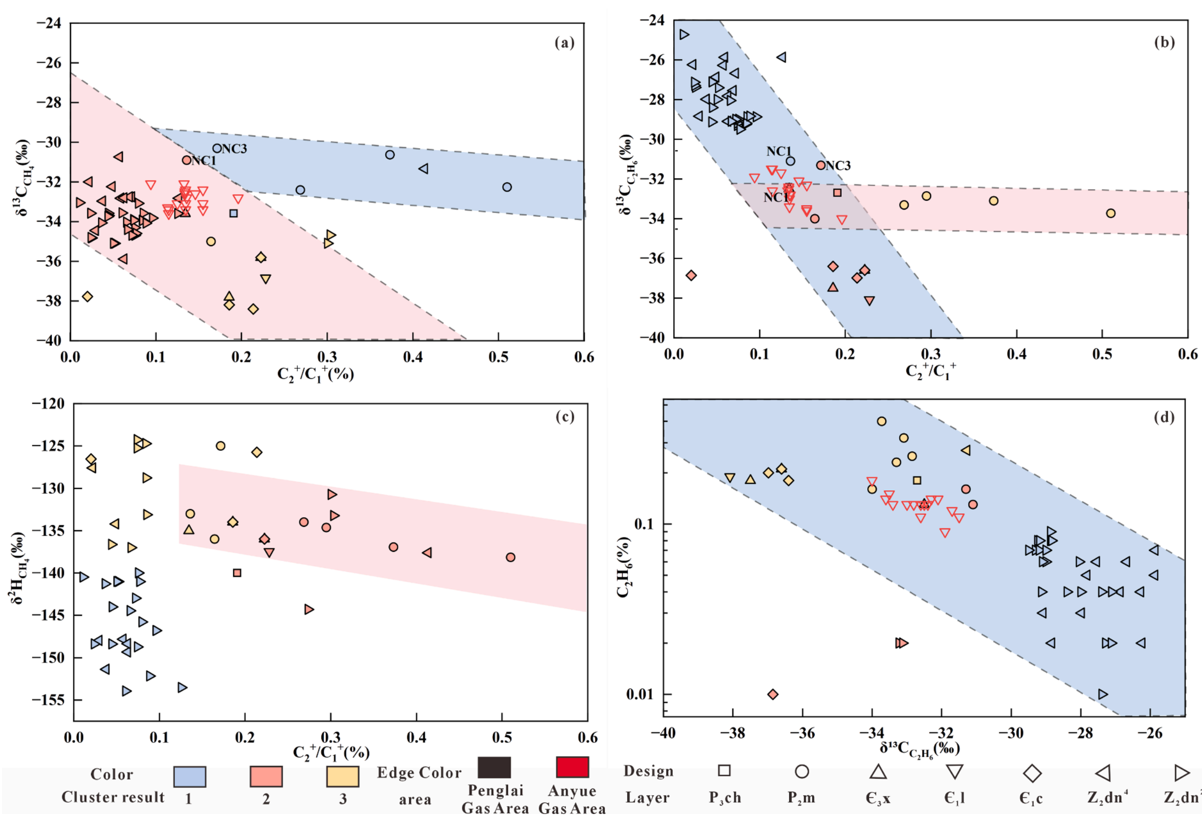

Fig. 10. Relationship between different carbon and hydrogen isotopic and maturity of Sinian – Permian system in Penglai gas area. (a) $\delta^{13}C_{CH_4}$ vs C_2^+/C_1^+; (b) $\delta^{13}C_{C_2H_6}$ vs C_2^+/C_1^+; (c) $\delta^2H_{CH_4}$ vs C_2^+/C_1^+; (d) C_2H_6 vs $\delta^{13}C_{C_2H_6}$. (data sources are listed in Table 1).

Specifically, the Sinian gas has a greater $\delta^{13}C_{CH_4}$ than the Cambrian gas, which aligns with the trend that older strata correlate with higher maturity and larger $\delta^{13}C_{CH_4}$ values. The maturity of Є$_1$l gas in the Anyue gas field surpasses that of Cambrian gas in the Penglai gas field, resulting in greater $\delta^{13}C_{CH_4}$ values. Although there is a positive correlation between maturity and $\delta^{13}C_{CH_4}$ in P$_2$m gas from the Penglai gas area, the variation in $\delta^{13}C_{CH_4}$ is minimal, and the overall $\delta^{13}C_{CH_4}$ values are greater (Fig. 10a), which is attributed to the greater $\delta^{13}C$ kerogen values of the P$_2$m-P$_2$q source rock (Fig. 9). Consequently, P$_2$m gas is influenced by both source rock and maturity.

Maturity significantly impacts $\delta^{13}C_{C_2H_6}$. In the Penglai gas area, natural gas from Z$_2$dn^2 and Z$_2$dn^4 exhibits lower C_2^+/C_1^+ ratios (0.010 % to 0.095 %) compared to the Є$_1$l gas (0.094 % to 0.196 %) of the Anyue gas field and is also lower than the Є$_3$x, Є$_1$l, and Є$_1$c gases (0.185 % to 0.228 %) from the Penglai gas area. As maturity increases, $\delta^{13}C_{C_2H_6}$ value increases accordingly(Fig. 10b). The Cambrian gas in the Penglai gas area largely stems from oil cracking in relatively early stages, whereas the Anyue gas field's gas is oil-cracking gas from later stages. Thus, the Sinian-Cambrian gas exhibits maturity control both horizontally and vertically. In the Penglai gas area, P$_2$m natural gas shows a broader variability in C_2^+/C_1^+ (0.136 % to 0.510 %), yet $\delta^{13}C_{C_2H_6}$ remains relatively consistent. The $\delta^{13}C_{C_2H_6}$ (–33.72 ‰ to −31.1 ‰) value of P$_2$m gas with lower maturity is similar to Є$_1$l $\delta^{13}C_{C_2H_6}$ (−34 ‰ to −31.5 ‰) of Anyue gas field with higher maturity (Fig. 10b). This phenomenon can be attributed to the greater kerogen $\delta^{13}C$ of the P$_2$m-P$_2$q source rocks, leading to a consistently greater $\delta^{13}C_{C_2H_6}$ in P$_2$m natural gas.

Regarding $\delta^2H_{CH_4}$, both Cambrian and P$_2$m natural gases exhibit an increase in $\delta^2H_{CH_4}$ as the C_2^+/C_1^+ ratio decreases (Fig. 10c). Although $\delta^2H_{CH_4}$ is also influenced by maturity, the effect is minimal.

In highly mature natural gas, early generated C_2H_6 tends to crack (Tian et al., 2007). Without further C_2H_6 generation, $\delta^{13}C_{C_2H_6}$ experiences Rayleigh distillation: $\delta^{12}C$-enriched C_2H_6 preferentially cracks due to lower activation energy, increasing the proportion of $\delta^{13}C_{C_2H_6}$ in the remaining C_2H_6 as maturity advances (Wu et al., 2016c). Thus, lower C_2H_6 content correlates with a greater $\delta^{13}C_{C_2H_6}$ (Fig. 10d). Sinian-Permian natural gas follows these $\delta^{13}C_{C_2H_6}$ fractionation patterns, with Z$_2$dn natural gas being more influenced by Rayleigh distillation. In contrast, P$_2$m and Cambrian natural gases are less affected. The C_2H_6 content of P$_2$m gas is similar to that of Є$_3$x, Є$_1$l, and Є$_1$c gases, yet it exhibits larger $\delta^{13}C_{C_2H_6}$ values (Fig. 10d).

5.3.3. *Hydrothermal and TSR impacts*

The higher H_2S and CO_2 contents in the Penglai gas area (Fig. 3b) suggest more intense TSR modification, although acidizing during formation testing may inflate CO_2 levels (Wei et al., 2015). Therefore, H_2S content and the Gas Sourness Index (GSI) $= H_2S/(H_2S + \sum C_n)$ are used to assess TSR impact, with a GSI > 0.01 generally indicating TSR alteration (Liu et al., 2019).

The $\delta^{13}C_{CH_4}$ signature exhibits a weak correlation with both GSI and H_2S levels (Fig. 11a, b). Since TSR has not progressed to the stage of reacting with CH_4, it is unlikely to affect $\delta^{13}C_{CH_4}$ value significantly.

In contrast, $\delta^{13}C_{C_2H_6}$ shows a strong positive correlation with GSI and H_2S (Fig. 11c, d). The natural gas from Z$_2$dn^2 and Z$_2$dn^4, which exhibit higher GSI, is more profoundly affected by TSR. Conversely, gas from Є$_1$c, Є$_1$l, and P$_2$m, with lower GSI, experiences less TSR modification. Consequently, $\delta^{13}C_{C_2H_6}$ values of the Z$_2$dn^2 and Z$_2$dn^4 samples are notably higher than those of the Є$_1$c, Є$_1$l, and P$_2$m samples, indicating that TSR exerts a more substantial influence on $\delta^{13}C_{C_2H_6}$.

As previously noted, the carbon isotope signatures of high-maturity natural gas typically exhibit carbon isotopic reversal. However, the natural gas from Z$_2$dn^2 and Z$_2$dn^4 displays a non-reversal pattern (Fig. 4a), likely due to the greater impact of TSR modification. The $\delta^{13}C_{C_2H_6}$ in these samples is anomalously enriched in ^{13}C as a result. Moreover, the $\delta^{13}C_{C_2H_6}$ in Z$_2$dn^2 and Z$_2$dn^4 is significantly influenced by fractionation, with the enrichment process being accelerated by fractionation effects. Consequently, this shifts the carbon isotope signature

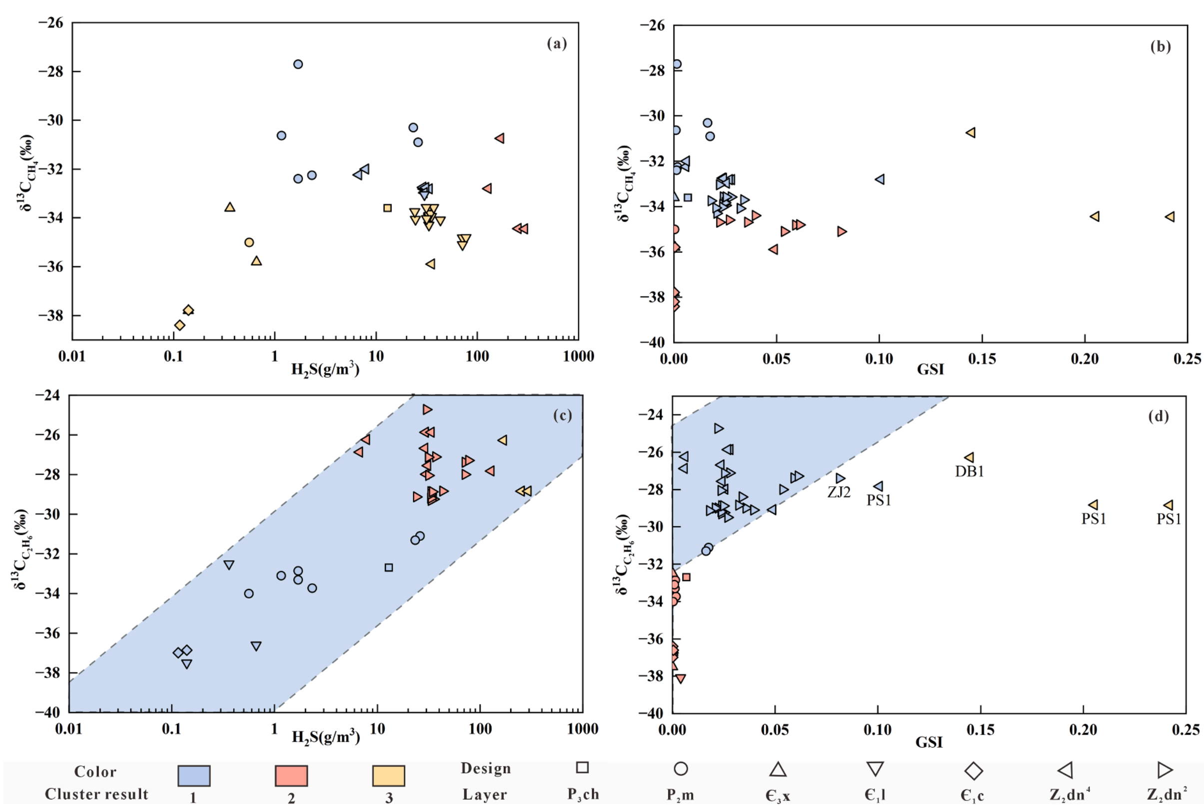

Fig. 11. Relationship between different carbon isotopic and TSR of Sinian – Permian system in Penglai gas area. (a) $\delta^{13}C_{CH_4}$ vs H_2S; (b) $\delta^{13}C_{CH_4}$ vs GSI; (c) $\delta^{13}C_{C_2H_6}$ vs H_2S; (d) $\delta^{13}C_{C_2H_6}$ vs GSI. (data sources are listed in Table 1).

from an expected reversal, attributable to high maturity and fractionation, to a non-reversal state.

5.3.4. Differences in the salinity of paleowater media during the depositional period

Several factors influence the $\delta^2H_{CH_4}$ of natural gas, including source rocks, maturity, the salinity of paleowater medium during source rock deposition, water involvement in pyrolysis reactions, and secondary modifications like TSR (Huang et al., 2019; Liu et al., 2019; Ni et al., 2019).

The $\delta^2H_{CH_4}$ of natural gas is influenced by the salinity of the paleowater medium during deposition, with higher salinity generally resulting in greater $\delta^2H_{CH_4}$. (Xia et al., 2015; Xie et al., 2021a) indicated that the Niutitang Formation, which shares a depositional period with Є$_1$q, had the highest paleowater salinity levels, ranging from 5.7 ‰ to 44.2 ‰. The Є$_1$c directly overlays the Є$_1$q, and its natural gas exhibits greater $\delta^2H_{CH_4}$ values (−136 ‰ to −123 ‰) (Fig. 4b and Fig. 10c), signifying a correlation with high salinity levels. In contrast, the Z$_2$dn^3 source rock's paleowater salinity ranges from 4.5 ‰ to 10.3 ‰, making the $\delta^2H_{CH_4}$ of natural gas of Z$_2$dn^2 and Z$_2$dn^4 generally lower than that of Є$_1$c. Thus, natural gas from Z$_2$dn^2 and Z$_2$dn^4 is marked by contributions from Z$_2$dn^3, characterized by lower $\delta^2H_{CH_4}$.

5.3.5. Analysis of hierarchical clustering

Unlike manual classification, machine-learning-based classification classifies natural gas samples based on data similarity, minimizing human interference. In our study, we found that hierarchical clustering can effectively classify natural gas based on geochemical information such as its origin, composition, and maturity.

Using $\delta^{13}C_{CH_4}$ and C_2^+/C_1^+ ratio, hierarchical clustering categorizes the samples into three clusters (Fig. 10a). Cluster "0″ primarily includes samples from P$_2$m, characterized by a greater $\delta^{13}C_{CH_4}$ due to its source rocks and a higher C_2^+/C_1^+ ratio reflecting greater maturity. In contrast, Clusters "2″ and "3″ mainly comprise samples from Z$_2$dn and Cambrian, respectively. The Z$_2$dn natural gas in Cluster "2″ exhibits higher maturity, resulting in a greater $\delta^{13}C_{CH_4}$. Cluster "1″ is mainly differentiated from the others by its source, while Clusters "2″ and "3″ are distinguished by maturity differences.

Using $\delta^{13}C_{C_2H_6}$ and C_2^+/C_1^+ ratio, hierarchical clustering also categorizes the samples into three clusters (Fig. 10b). As before, P$_2$m gas samples are mainly distinguished by their source, while Z$_2$dn and Cambrian gas samples are differentiated by maturity. Notably, in the NC1 well, the $\delta^{13}C_{C_2H_6}$ of P$_2$m natural gas is greater and falls within the Sinian gas region, and the $\delta^{13}C_{C_2H_6}$ of Є$_1$x is greater than that of other Cambrian gases. This may be attributed to a greater contribution of P$_2$m-P$_2$q source rocks.

Using $\delta^2H_{CH_4}$ and C_2^+/C_1^+ ratio, hierarchical clustering categorizes the samples into three clusters (Fig. 10c). One cluster consists of parts of Z$_2$dn gas samples with low $\delta^2H_{CH_4}$ (<-140 ‰), which is related to greater contribution from the Z$_2$dn^3 source rock (lower $\delta^2H_{CH_4}$ due to salinity). Another cluster with a high $\delta^2H_{CH_4}$ value ($\delta^2H_{CH_4} > -136$ ‰) includes samples from Z$_2$dn, P$_2$m and Cambrian, which are related to a greater contribution of Є$_1$q source. Most of the remaining gas samples from P$_2$m and Cambrian are grouped into one, which is greatly affected by maturity.

Similarly, to illustrate the effect of TSR, hierarchical clustering was used to group the samples by combining H_2S content, GSI and carbon isotope. Since TSR has little effect on methane carbon isotope, it is not possible to effectively distinguish natural gas based on H_2S content, GSI and carbon isotope (Fig. 11a, b). Using $\delta^{13}C_{C_2H_6}$, GSI, and H_2S content, hierarchical clustering identified the Z$_2$dn gas samples (PS1, DB1 well) strongly modified by TSR. Other Z$_2$dn gas samples were also modified by TSR, while the Cambrian and P$_2$m gas samples were basically not modified by TSR (Fig. 11c, d).

5.4. End-member method for calculating the contribution of source rocks

As previously discussed, $\delta^2H_{CH_4}$ levels are primarily influenced by the salinity of the paleowater medium during source rock deposition. Consequently, natural gas from the Є$_1$q source rock in the Penglai gas area exhibits greater $\delta^2H_{CH_4}$, while that from the Z$_2$dn^3 source rock has lower $\delta^2H_{CH_4}$. By referring to prior research (Zhao et al., 2021), the end-member method, based on $\delta^2H_{CH_4}$, was employed to determine the proportional contributions of Z$_2$dn^3 source rock to the natural gas in Z$_2$dn^2 and Z$_2$dn^4 (Formula 1).

$$C_Z = \left(E_{\epsilon}\delta^2H_{CH_4} - \delta^2H_{CH_4}\right) / \left(E_{\epsilon}\delta^2H_{CH_4} - E_Z\delta^2H_{CH_4}\right) \tag{1}$$

C_z is the Contribution ratio of Z$_2$dn^3 source rock; $E_Є\delta^2H_{CH_4}$ is the $\delta^2H_{CH_4}$ end-member value of Є$_1$q source; $E_Z\delta^2H_{CH_4}$ is $\delta^2H_{CH_4}$ end-member value of Z$_2$dn^3 source.

Z$_2$dn natural gases $\delta^2H_{CH_4}$ span from −162.1 ‰ to −121.4 ‰, with only one sample exceeding −156 ‰. Consequently, −156 ‰ was selected as Z$_2$dn^3 end-member value, and samples with $\delta^2H_{CH_4}$ below −156 ‰ were attributed 100 % to Z$_2$dn^3 source rocks. The Cambrian natural gas from Є$_1$c and Є$_1$l, which constitutes the Є$_1$q source rock, displays $\delta^2H_{CH_4}$ values between −138 ‰ and −123 ‰. Hierarchical clustering identified −136 ‰ as the demarcation for two types of Z$_2$dn gas, with only two Cambrian natural gas samples surpassing −136 ‰. Thus, −136 ‰ was chosen as the Є$_1$q end-member value, and samples with $\delta^2H_{CH_4}$ above −136 ‰ were attributed 100 % to Є$_1$q source rock.

The calculations reveal that, excluding samples exceeding the end-member values, the Sinian source rocks contribute more significantly to the natural gas in Z$_2$dn^2, with contributions ranging from 11.98 % to 90.64 %. In contrast, their contribution to Z$_2$dn^4 is somewhat lower, varying from 0.98 % to 78.96 %. Vertically, the Z$_2$dn^2, being farther from the Є$_1$q, exhibits a higher contribution from Sinian source rock, whereas Z$_2$dn^4 shows a lower contribution. Laterally, the proportion of Sinian source rock contribution generally increases as one moves away from the Deyang-Anyue rift trough towards the interior of the platform. Additionally, there is a trend of increasing Z$_2$dn^3 source rock contribution towards the southwest, which correlates with variations in the thickness of the Z$_2$dn^3 source rocks (Fig. 12).

Considering the contribution of the P$_2$m-P$_2$q source rocks to the P$_2$m natural gas, the distinct $\delta^{13}C_{C2H6}$ differences between Cambrian and Permian natural gases, coupled with stronger correlation with the source, led to the selection of $\delta^{13}C_{C_2H_6}$ as the end-member for calculating P$_2$m-P$_2$q source rock contributions. Following a comparative analysis of gas sources, the natural gas in well NC1 exhibits a greater contribution from the P$_2$m-P$_2$q source rock. Consequently, −29 ‰ was selected as the end-member value for the P$_2$m-P$_2$q source rocks. The average $\delta^{13}C_{C_2H_6}$ value of −36 ‰ for Є$_1$c was adopted as the Cambrian end-member value (Formula 2).

$$C_P = \left(E_{\epsilon}\delta^{13}C_{C_2H_6-} - \delta^{13}C_{C_2H_6}\right) / \left(E_{\epsilon}\delta^{13}C^2H^6 - E_P\delta^{13}C_{C_2H_6}\right) \tag{2}$$

C_P is the contribution ratio of Permian source rocks; $E_Є\delta^{13}C_{C_2H_6}$ is$\delta^{13}C_{C_2H_6}$ endmember value of Є$_1$q source; $E_P\delta^{13}C_{C_2H_6}$ is$\delta^{13}C_{C_2H_6}$ end-member value of P$_2$m-P$_2$q source.

The calculations indicate that the contributions of P$_2$m-P$_2$q source rock to the P$_2$m natural gas in JT1 and ZJ1 wells are relatively small, ranging from 32.43 % to 36.26 %. In contrast, the contributions of P$_2$m-P$_2$q source rock to the P$_2$m natural gas in NC1 and NC3 wells are substantial, varying from 68.92 % to 87.58 %. Additionally, the Є$_3$x natural gas in the NC1 well exhibits a moderate to high P$_2$m-P$_2$q source rock contribution, at 52.7 %.

5.5. Differential natural gas accumulation patterns in multi-strata

5.5.1. Multi-source supply of hydrocarbons

In the Penglai gas area, the Z$_2$dn^3, Є$_1$q, and P$_2$m-P$_2$q represent three

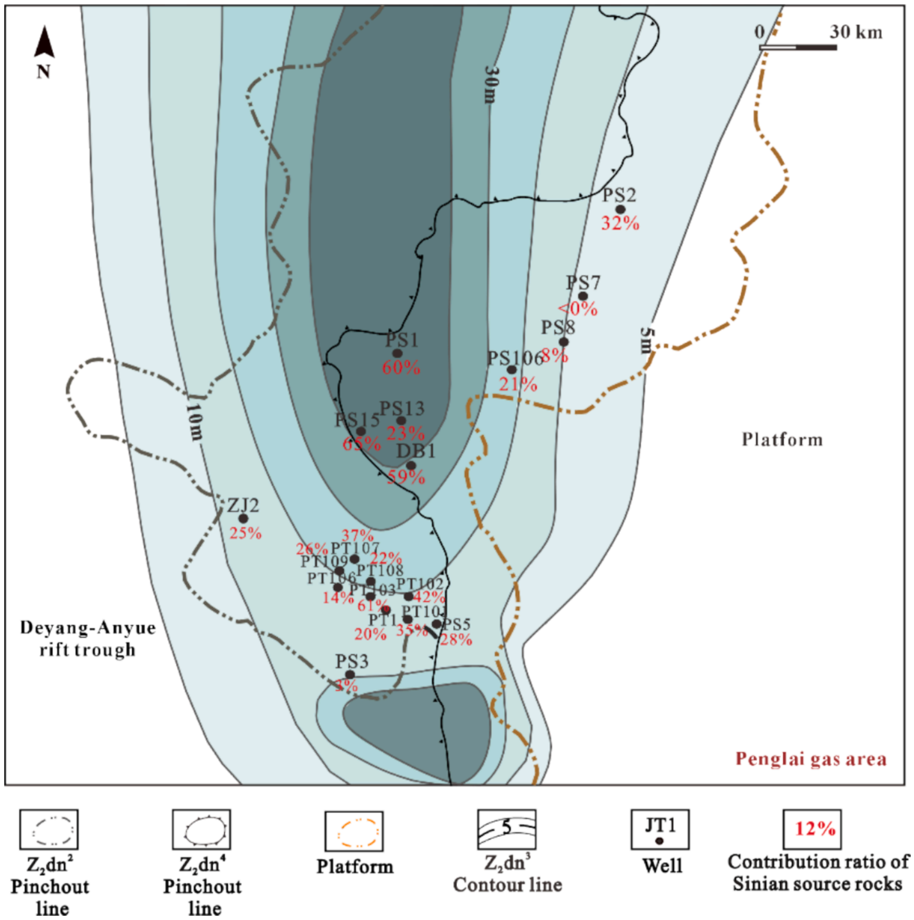

Fig. 12. Contribution ratio of Sinian source rocks in Penglai gas area and thickness distribution map of Z_2dn^3.

main sets of source rocks developed vertically within the Sinian-Permian system (Fig. 13 and 14). Despite the over-maturity of the Z_2dn^3 source rocks (R_{oe} approximately 3.0 %), recent studies suggested the upper R_o limit for source rock to generate hydrocarbon could reach 3.5 % (Zhang et al., 2021; Zhao et al., 2021). This suggests that Z_2dn^3 source rock still retains some hydrocarbon generation potential and contributes to Z_2dn^2 and Z_2dn^4 natural gas. As the primary source rock, $Є_1q$ plays a significant role in the Sinian-Permian gas accumulation due to its considerable thickness and extensive distribution, leading to multi-strata natural gas accumulation. The contribution of P_2m-P_2q source rocks to

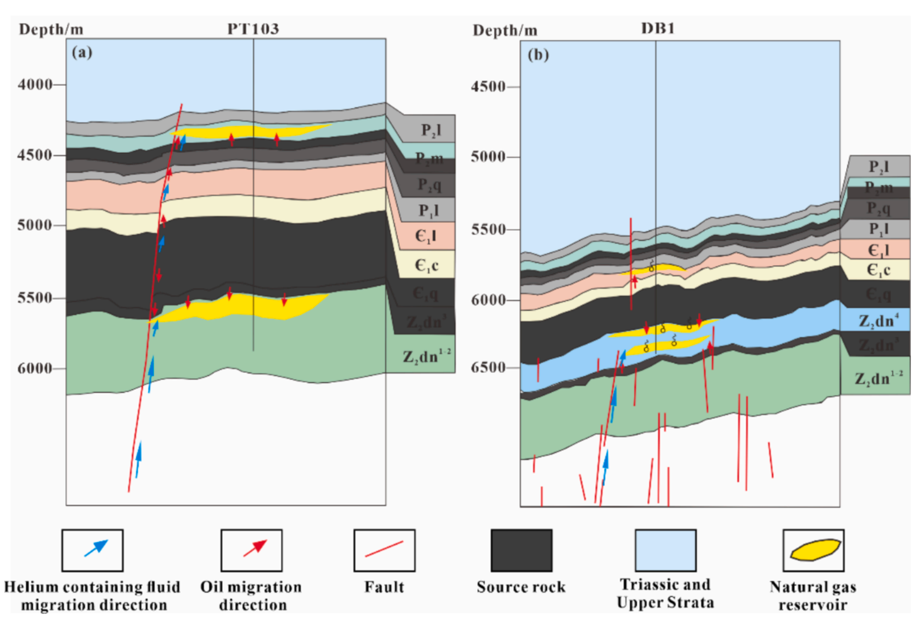

Fig. 13. Differential accumulation mode of Sinan-Permia system of PT103 well(a) and DB1 well(b) in Penglai gas area.

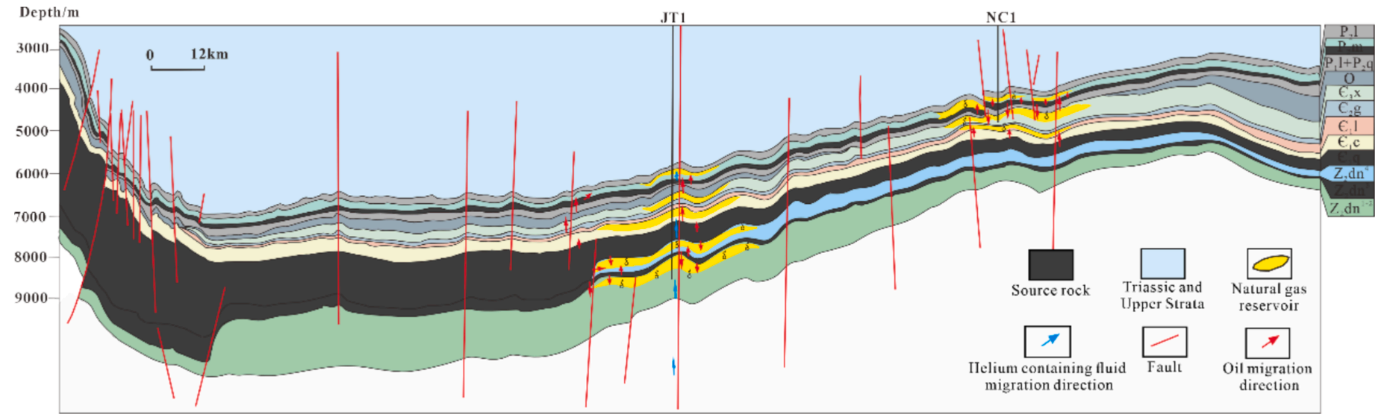

Fig. 14. Differential accumulation mode of Sinan-Permia system of JT1well and NC1 well in Penglai gas area.

hydrocarbons varies and is influenced by strike-slip faults. Overall, P_2m natural gas in the Penglai gas area receives contributions from the P_2m-P_2q source rocks. Moreover, the $Є_3$x of the NC1 well also shows contributions from the P_2m-P_2q source rocks.

5.5.2. Hydrothermal influences on differential accumulation

In the Penglai gas area, the Z_2dn gas accumulation is predominantly influenced by TSR. Despite the absence of gypsum-salt layers in Z_2dn and adjacent formations, deep hydrothermal fluids significantly impact the accumulation by providing sulfur necessary for TSR. Shallower strata, including the Cambrian $Є_1$c, $Є_1$l, $Є_3$x, and Permian P_2m, exhibit minimal to no effects from TSR. This limited influence is due to the extensive distribution of $Є_1$q shale, which allows hydrothermal fluids to more substantially affect strata beneath $Є_1$q. As a result, natural gas accumulations in the Cambrian system and P_2m strata differ markedly from those in the Z_2dn accumulation. There is a clear distinction in gas accumulation between the upper and lower $Є_1$q, with the lower strata being more significantly impacted by the hydrothermal influences and TSR. This delineation highlights the role of geological barriers and fluid pathways in shaping the characteristics and distribution of natural gas in the region.

5.5.3. Strike-slip faults control on gas accumulation

In the Penglai gas area, a series of natural gas accumulations span from the Sinian to Permian, including the Z_2dn^2, Z_2dn^4, $Є_1$c, $Є_1$l, $Є_3$x, and P_2m. These accumulations, which extend across multi-strata and extensive geologic time frames, exhibit distinct geochemical signatures and geological conditions, indicating varied accumulation characteristics. The development of these accumulations is significantly influenced by strike-slip faults, which interconnect multiple sources and reservoirs. This connectivity facilitates the development of gas accumulations in the Permian and Sinian systems that contain measurable amounts of He and N_2.

He and N_2 exhibit a correlated presence within certain accumulations, sharing similar origins and migration pathways. These gases can be generated from underlying granite or highly mature, radioactive source rocks and are transported to gas reservoirs by deep fluids (Qin et al., 2024). Deep-seated faults that intersect the basement granite play a crucial role by serving as conduits for He and N_2 fluids, establishing a direct link to the gas accumulations. As a result, gas reservoirs with similar He and N_2 contents are likely to have correlated accumulation processes.

The PT103 well exhibits notable gas accumulations with a high He (0.38 %) and N_2 (31.85 %) content in the Z_2dn^2, contrasting with the absence of such accumulations in the Cambrian, and lower levels of He (0.01 %) and N_2 (0.53 %) in the P_2m (Table 1). This well is situated near the first-order strike-slip fault F_I-10, which extends from the Z_2dn base to the Upper Permian (Fig. 13a), serving as a conduit for the migration of He and N_2-enriched fluids from the basement granite to the Z_2dn^2 and P_2m. Conversely, the Cambrian exhibits pronounced faulting, correlating with poor gas preservation and a lack of natural gas accumulations (Fig. 13a). Moreover, the PT103 well, located at the Z_2dn^2 platform margin and close to the source rock, has experienced thermochemical alteration of organic matter leading to elevated N_2 levels. The ZJ2 well is similar to PT103, but due to its proximity to the Deyang-Anyue rift trough, Z_2dn^2 is enveloped by thicker source rocks, resulting in a higher N_2 (93.8 %) content. Consequently, the PT103 well and ZJ2 well are characterized by a unique mode of natural gas enrichment in the upper and lower strata (P_2m and Z_2dn), with He and N_2-rich gas accumulations.

Using DB1 as a reference, the Z_2dn^4 interval shows lower He (0.04 %) and N_2 (0.52 %) contents compared to the Z_2dn^2 in PT103 well. A notable discrepancy is the high N_2 levels (29.2 %) with an absence of He in DB1 (Table 1). The seismic profile reveals that the development of basement faults in the deep part of the DB1 well leads to stronger hydrothermal activity, resulting in pronounced TSR characteristics. Meanwhile, faults within the DB1 well predominantly occur in Z_2dn and its lower reaches, with minimal presence in Cambrian, and lacking the continuous first-order faults in PT103 (Fig. 13b). Consequently, the Z_2dn^4 in DB1 has lower He levels, while the upper strata's contact with highly mature $Є_1$q source rock introduces elevated N_2 content. Therefore, DB1 exhibits an accumulation mode rich in N_2, with some helium presence and abundant natural gas in the middle and lower strata (Є and Z_2dn) (Fig. 13b).

The carbon isotope signatures of natural gas from the P_2m and $Є_3$x in the NC1 well diverge from those in other wells. Gas-source correlation indicates a greater influence from P_2m-P_2q source rock and a reduced contribution from the $Є_1$q for P_2m natural gas in NC1. This variance is linked to the distribution of strike-slip faults (Fig. 14). Around the NC1 well, these faults are primarily developed in the $Є_3$x, P_2m, and overlying strata, with a scarcity of prominent faults bridging the Sinian to Permian. Consequently, hydrocarbons from the P_2m-P_2q source rock not only accumulate in the P_2m but also migrate downwards along these strike-slip faults, leading to accumulations in both the $Є_3$x and P_2m, thus creating a gas accumulation mode rich in natural gas in the upper and middle strata (P_2m and Є).

The JT1 well presents a contrast; it is located near a first-order fault that spans from the basement to the Upper Triassic, facilitating the vertical migration of hydrocarbons from the $Є_1$q across multi-strata. This mode has resulted in the JT1 well having a multi-strata gas accumulation from the Sinian-Permian, creating a gas accumulation mode rich in natural gas in the upper, middle, and lower strata (P_2m, Є and Z_2dn).

6. Conclusion

The Sinian-Permian natural gas in the Penglai gas area primarily consists of dry gas derived from oil cracking, exhibiting significant variations in composition, carbon isotopes, and hydrogen isotopes. The gas in Z_2dn^2 and Z_2dn^4 is characterized by high non-hydrocarbon content, low C_2H_6, greater $\delta^{13}C_{C_2H_6}$, and lower $\delta^2H_{CH_4}$. In contrast, $Є_1l$ and $Є_1c$ show the opposite traits. The P_2m gas, however, is marked by high C_2H_6, greater $\delta^{13}C_{C_2H_6}$, and greater $\delta^2H_{CH_4}$.

The $\delta^{13}C_{CH_4}$ and $\delta^{13}C_{C_2H_6}$ of the Sinian-Permian gas in the Penglai gas area are influenced by the maturity level, with the C_2H_6 Rayleigh distillation also impacting $\delta^{13}C_{C2H6}$ due to higher maturity. The $\delta^{13}C_{C_2H_6}$ of Z_2dn^2 and Z_2dn^4 gas is affected by hydrothermal fluid and TSR, whereas the $\delta^{13}C_{CH_4}$ and $\delta^{13}C_{C_2H_6}$ of P_2m gas are influenced by the source. The positive carbon isotope sequence ($\delta^{13}C_{CH_4} < \delta^{13}C_{C_2H_6}$) in Z_2dn^2 and Z_2dn^4 is linked to C_2H_6 Rayleigh distillation and TSR. The $\delta^2H_{CH_4}$ is associated with the paleowater salinity during the deposition of source rock, with the $\delta^2H_{CH_4}$ of Cambrian and P_2m gas being affected by maturity.

The Z_2dn^2 and Z_2dn^4 natural gas received contributions from the Sinian source rocks, with a higher Sinian contribution in Z_2dn^2 (90.64 % to 11.98 %) and a slightly lower contribution in Z_2dn^4 (78.96 % to 0.98 %). The gas in $Є_1c$, $Є_1l$, $Є_3x$, and P_2m is predominantly sourced from the $Є_1q$. In NC1 and NC3 wells, the P_2m gas is mainly derived from the P_2m-P_2q source rock (68.92 % to 87.58 %). The $Є_3x$ in NC1 also shows a significant contribution from the P_2m-P_2q source rock, at 52.7 %.

The natural gas accumulation in the Penglai gas area has resulted from vertical differential accumulation, with different layers enriched in natural gas. This accumulation mode is shaped by multiple factors: diverse hydrocarbon sources, the impact of deep hydrothermal activity, and the control exerted by strike-slip faults. These geological and geochemical processes contribute to the distinct distribution and enrichment of natural gas across various strata in the region.

CRediT authorship contribution statement

Zezhang Song: Writing – review & editing, Supervision, Investigation. **Ziyu Zhang:** Writing – original draft, Methodology, Investigation, Data curation. **Bing Luo:** Resources, Project administration. **Wenjin Zhang:** Resources, Project administration. **Changqi Liu:** Investigation, Data curation. **Xingwang Tian:** Resources, Project administration. **Dailin Yang:** Resources, Project administration. **Luya Wu:** Project administration. **Bingfei Ge:** Data curation. **Shigui Jin:** Data curation. **Jiutao Yuan:** Data curation.

Declaration of competing interest

The authors declare that they have no known competing financial interests or personal relationships that could have appeared to influence the work reported in this paper.

Acknowledgements

This research was financially sponsored by the General Program of the National Natural Science Foundation of China (Grant No. 42272161), Ministry of Science and Technology (Grant No. 2024YFE0114000), China University of Petroleum, Beijing (Grant No. 2462023BJRC023). We would also thank PetroChina Southwest Oil & Gas Field Company for providing core samples and necessary data.

Data availability

Data will be made available on request.

References

Banner, J.L., 1995. Application of the trace element and isotope geochemistry of strontium to studies of carbonate diagenesis. Sedimentology 42, 805–824.
Cai, C., Worden, R.H., Bottrell, S.H., Wang, L., Yang, C., 2003. Thermochemical sulphate reduction and the generation of hydrogen sulphide and thiols (mercaptans) in Triassic carbonate reservoirs from the Sichuan Basin, China. Chemical Geology 202, 39–57.
Chen, S., Huang, H., Zhang, B., Xie, Z., 2017. Difference in gas generation from thermal cracking of oil within reservoir and from residual bitumen within source rock and its geological significance. Natural Gas Geoscience 28, 1375–1384.
Cheng, A., Sherwood Lollar, B., Gluyas, J.G., Ballentine, C.J., 2023. Primary N_2–He gas field formation in intracratonic sedimentary basins. Nature 615, 94–99.
Dai, J., 1993. Characteristics of hydrocarbon isotopes in natural gas and identification of various types of natural gas. Natural Gas Geoscience 1–40.
Fairchild, I.J., Spiro, B., 1987. Petrological and isotopic implications of some contrasting Late Precambrian carbonates, NE Spitsbergen. Sedimentology 34, 973–989.
Fang, X., Deng, B., Geng, A., Liu, S., Wang, P., Liang, X., Li, Y., Cheng, B., Jiang, W., Wu, L., 2024. Geochemical properties, mechanism of formation, and source of solid bitumen in the Ediacaran Dengying formation from the central to northern Sichuan Basin. China. Marine and Petroleum Geology 159, 106573.
Fu, X., Chen, Y.N., Luo, B., Li, W., Liu, R., Wang, X., He, Y., Gu, M., Jiang, H., 2022. Evaluation of source rocks and petroleum system of the Lower Cambrian Maidiping formation-Qiongzhusi formation in the middle-upper Yangtze region. China Petroleum Exploration 27, 103.
Fu, X., Zhang, B., Wang, Z., Lei, M., Zhang, J., Guan, S., Li, W., Zhong, Y., Gu, M., Chen, T., 2023. Strike-slip faults in central and western Sichuan Basin and their control functions on hydrocarbon accumulation. Earth Science 48, 2221–2237.
Han, C., Lin, C., Lu, X., Tian, J., Ren, L., Ma, C., 2019. Petrological and geochemical constraints on fluid types and formation mechanisms of the Ordovician carbonate reservoirs in Tahe Oilfield, Tarim Basin, NW China. Journal of Petroleum Science and Engineering 178, 106–120.
He, K., Zhang, S., Wang, X., Mi, J., Mao, R., Hu, G., 2013. Effect of gas generation from in-situ cracking of residual bitumen in source on hydrocarbon generation from organic matter. Acta Petrolei Sinica 34, 57.
Huang, S., Shufu, D., Zecheng, W., Jiang, Q., Jiang, H., Wang, S., Qingfu, F., Huang, T., Miao, Y., Mengyi, R., 2019. Affecting factors and application of the stable hydrogen isotopes of alkane gases. Petroleum Exploration and Development 46, 518–530.
Jiang, N., 2015. The hydrothermal activity of the Sinian Dengying Formation in the Gaoshiti Moxi area of central Sichuan basin and its impact on reservoirs. Southwest Petroleum University, Chengdu, pp. 20–30.
Jiang, Y., Gu, Y., Zhu, X., Xu, W., Xiao, Y., Li, J., 2017. Hydrothermal dolomite reservoir facies in the Sinian Dengying Fm, central Sichuan Basin. Natural Gas Industry B 4, 287–293.
Jiedong, Y., Weiguo, S., Zongzhe, W., Yaosong, X., Xiancong, T., 1999. Variations in Sr and C isotopes and Ce anomalies in successions from China: evidence for the oxygenation of Neoproterozoic seawater? Precambrian Research 93, 215–233.
Lei, R., Xiong, Y., Li, Y., Zhang, L., 2018. Main factors influencing the formation of thermogenic solid bitumen. Organic Geochemistry 121, 155–160.
Li, Q., Liu, G., Song, Z., Sun, M., Zhu, L., Tian, X., Ma, K., Yang, D., Wang, Y., Cao, Y., You, F., 2022. Influence of tectonie evolution of the northern slope in the central Sichuan paleo-uplift on the Sinian-Cambrian hydrocarbon accumulations. Peroleum Geology & Experiment 44, 997–1007.
Li, K., Song, J., Liu, S., Yang, D., Li, Z., Jin, X., Ren, J., Zhao, L., Xia, S., Tian, L., Wang, S., Zhang, Y., 2024. Element significance of microbial rock fabric in Late Ediacaran strata from the Sichuan Basin. Acta Sedimentologica Sinica 42, 64–83.
Liang, X., Liu, S., Wang, S., Deng, B., Zhou, S., Ma, W., 2019. Analysis of the oldest carbonate gas reservoir in China—New geological significance of the Dengying gas reservoir in the Weiyuan structure, Sichuan Basin. Journal of Earth Science 30, 348–366.
Liu, Q., Jin, Z., Li, J., Hu, A., Bi, C., 2012. Origin of marine sour natural gas and gas-filling model for the Wolonghe Gas Field, Sichuan Basin, China. Journal of Asian Earth Sciences 58, 24–37.
Liu, Q., Zhu, D., Jin, Z., Liu, C., Zhang, D., He, Z., 2016. Coupled alteration of hydrothermal fluids and thermal sulfate reduction (TSR) in ancient dolomite reservoirs – An example from Sinian Dengying Formation in Sichuan Basin, southern China. Precambrian Research 285, 39–57.
Liu, Q., Wu, X., Wang, X., Jin, Z., Zhu, D., Meng, Q., Huang, S., Liu, J., Fu, Q., 2019. Carbon and hydrogen isotopes of methane, ethane, and propane: A review of genetic identification of natural gas. Earth-Science Reviews 190, 247–272.
Liu, Q., Lu, X., Fan, J., Liu, S., Ma, X., Dai, B., Gui, L., Chen, W., 2022a. Evidence and controlling factors of thermochemical sulfate reduction in the Sinian gas reservoirs , Sichuan Basin. Natural Gas Geoscience 33, 929–943.
Liu, W., Wang, J., TengGe'er, Zhang, D., Rao, D., Tao, C., 2010. New knowledge of gas source rocks in them arine sequences of South China and relevant index system for tracing. Oil & Gas Geology 31, 819–825.
Liu, Q., Wu, X., Jia, H., Ni, C., Zhu, J., Miao, J., Zhu, D., Meng, Q., Peng, W., Xu, H., 2022b. Geochemical characteristics of helium in natural gas from the Daniudi Gas Field, Ordos Basin. Central China. Frontiers in Earth Science 10, 10.
Machel, H.G., Krouse, H.R., Sassen, R., 1995. Products and distinguishing criteria of bacterial and thermochemical sulfate reduction. Applied Geochemistry 10, 373–389.
Milkov, A.V., Etiope, G., 2018. Revised genetic diagrams for natural gases based on a global dataset of >20,000 samples. Organic Geochemistry 125, 109–120.
Ni, Y., Liao, F., Gao, J., Chen, J., Yao, L., Zhang, D., 2019. Hydrogen isotopes of hydrocarbon gases from different organic facies of the Zhongba gas field, Sichuan Basin, China. Journal of Petroleum Science and Engineering 179, 776–786.
Peng, W., Liu, Q., Zhang, Y., Jia, H., Zhu, D., Meng, Q., Wu, X., Deng, S., Ma, Y., 2022. The first extra-large helium-rich gas field identified in a tight sandstone of the Dongsheng Gas Field, Ordos Basin, China. Science China Earth Sciences 65, 874–881.

Qin, S., Zhou, G., Li, W., Hou, Y., Lü, F., 2016. Geochemical evidence of water-soluble gas accumulation in the Weiyuan gas field, Sichuan Basin. Natural Gas Industry B 3, 37–44.
Qin, S., Zhou, G., Li, J., Tao, G., Zhao, Z., 2024. The coupling action of helium and nitrogen enrichment and its significance. Journal of Natural Gas Geoscience 9, 1–12.
Shuai, Y., Zhang, S., Hu, G., Li, W., Wang, T., Qin, S., 2019. Thermochemical sulphate of Sinian and Cambrian natural gases in the Gaoshiti-Moxi area, Sichuan Basin, and its enlightment for gas sources. Acta Geologica Sinica 93, 1754–1766.
Shuai, Y., Liu, K., Hu, G., Wang, T., Tian, X., Zhang, B., Chen, Z., 2021. Gas accumulation mechanisms of the Sinian reservoir in the Sichuan Basin and their significance for deep gas exploration. Acta Geologica Sinica 95, 3400–3412.
Shuai, Y., Li, J., Tian, X., Chen, Z., Zhang, B., Wei, C., 2023. Accumulation mechanism of Sinian to Triassic gas reservoirs in the central and western Sichuan Basin and their significance for oil and gas prospecting. Acta Geologica Sinica 97, 1526–1543.
Song, J., Jin, X., Luo, Z., Liu, S., Liu, S., Ma, X., Li, Z., Lu, X., Zhao, L., Li, K., Ren, J., Tian, L., Deng, H., 2024. Depositional model of the Member Deng-2 marginal microbial mound-bank complex of the Dengying Formation in the southwestern Sichuan Basin, SW China: Implications for the Ediacaran microbial mound construction and hydrocarbon exploration. Petroluem Science 21, 806–822.
Song, Z., Liu, G., Luo, B., Zeng, Q., Tian, X., Dai, X., Jiang, R., Wang, Y., Li, Q., Zhao, J., Abula, A., Zang, J., 2021. Logging evaluation of solid bitumen in tight carbonate in deepburied and ultra-deep-buried strata of the Central Sichuan Basin. Acta Geologica Sinica 39, 197–211.
Swart, P.K., 2015. The geochemistry of carbonate diagenesis: the past, present and future. Sedimentology 62, 1233–1304.
Tian, H., Xiao, X., Li, X., Xiao, Z., Shen, J., Liu, D., 2007. Comparison of gas generation and carbon isotope fractionation of methanefrom marine kerogen- and crude oil-cracking gases. Geochimica 71–77.
Wang, W., Ren, L., Liang, J., Tang, S., Yuan, H., Li, Y., 2022b. Characteristics and hydrocarbon generation potential of Middle Permian marine source-rocks in central Sichuan Basin Natural Gas Geoscience 33, 369-380.
Wang, X., Liu, Q., Liu, W., Li, X., Tao, C., Li, X., Zhao, D.O., Zhang, J., Zhu, D., Meng, Q., Xu, H., Wu, X., 2023. Helium accumulation in natural gas systems in Chinese sedimentary basins. Marine and Petroleum Geology 150, 11.
Wang, W.-Y., Pang, X.-Q., Wang, Y.-P., Chen, Z.-X., Li, C.-R., Ma, X.-H., 2022a. Hydrocarbon expulsion model and resource potential evaluation of high-maturity marine source rocks in deep basins: Example from the Ediacaran microbial dolomite in the Sichuan Basin, China. Petroleum Science 19, 2618–2630.
Wei, G., Wang, D., Wang, X., Li, J., Li, Z., Xie, Z., Cui, H., Wang, Z., 2014a. Characteristics of noble gases in the large Gaoshiti-Moxi gas field in Sichuan Basin, SW China. Petroleum Exploration and Development 41, 585–590.
Wei, G., Xie, Z., Bai, G., Li, J., Wang, Z., Li, A., Zhisheng, L., 2014b. Organic geochemical characteristics and origin of natural gas in the Sinian-Lower Paleozoic reservoirs, Sichuan Basin. Natural Gas Industry 34, 44–49.
Wei, G., Xie, Z., Song, J., Yang, W., Wang, Zhihong, Li, J., Wang, D., Li, Z., Xie, W., 2015. Features and origin of natural gas in the Sinian–Cambrian of central Sichuan paleo-uplift, Sichuan Basin, SW China. Petroleum Exploration and Development 42, 768–777.
Wei, G., Xie, Z., Yang, Y., Li, J., Yang, W., Zhao, L., Yang, C., Zhang, L., Xie, W., Jiang, H., Li, Z., Li, J., Guo, J., 2022. Formation conditions of Sinian–Cambrian large lithologic gas reservoirs in the North Slope area of central Sichuan Basin, SW China. Petroleum Exploration and Development 49, 963–976.
Whiticar, M.J., 1999. Carbon and hydrogen isotope systematics of bacterial formation and oxidation of methane. Chemical Geology 161, 291–314.
Whiticar, M.J., 1994. Correlation of natural gases with their sources. In: Magoon, L.B., Dow, W.G. (Eds.), The Petroleum System—From Source to Trap. American Association of Petroleum Geologists, pp. 261–283.
Wu, J., Liu, S., Wang, G., Zhao, Y., Sun, W., Song, J., Tian, Y., 2016a. Multi-stage hydrocarbon accumulation and formation pressure evolution in Sinian Dengying Formation-Cambrian Longwangmiao Formation, Gaoshiti-Moxi structure, Sichuan Basin. Journal of Earth Science 27, 835–845.
Wu, X., Liu, Q., Liu, G., Ni, C., 2019. Genetic types of natural gas and gas-source correlation in different strata of the Yuanba gas field, Sichuan Basin, SW China. Journal of Asian Earth Sciences 181, 103906.
Wu, W., Luo, B., Luo, W., Wang, W., 2016b. Further discussion about the origin of natural gas in the Sinian of central Sichuan paleo-uplift, Sichuan Basin, China. Journal of Natural Gas Geoscience 1, 353–359.
Wu, W., Luo, C., Zhang, J., Liu, W., 2016c. Evolution law and genesis of ethane carbon isotope of oil type gas. Acta Petrolei Sinica 37, 1463.
Xia, W., Yu, B., Sun, M., 2015. Depositional setting and enrichment mechanism of organic matter of the black shales of Niutitang Formation at the bottom of Lower Cambrian, in Well Yuke 1, southeast Chongqing. Mineraloogy and Petrology 35, 70–80.
Xie, Z., Li, Z., Wei, G., Li, J., Wang, D., Wang, Z., Dong, C., 2016. Experimental research on the potential of sapropelic kerogen cracking gas and discrimination of oil cracking. Natural Gas Geoscience 27, 1057–1066.
Xie, Z., Yang, C., Dong, C., Dai, X., Zhang, L., Guo, J., Guo, Z., Li, Z., Li, J., Qi, X., 2020. Geochemical characteristics and genesis of Middle Devonian and Middle Permian natural gas in Sichuan Basin, China. Natural Gas Geoscience 31, 447–461.
Xie, Z., Li, J., Yang, C., Tian, X., Zhang, L., Li, J., Li, Z., Guo, J., Xie, W., Guo, Z., Qi, X., Hao, A., 2021a. Geochemical characteristics of Sinian-Cambrian natural gas in central Sichuan paleo-uplift and exploration potential of Taihe gas area. Natural Gas Industry 41, 1–14.
Xie, Z., Wei, G., Li, J., Xu, L., Zhang, L., Li, J., Li, Z., Wu, S., Guo, Z., Hao, A., 2021b. Geochemical characteristics and accumulation pattern of gas reservoirs of the Sinian-Permian in central Sichuan uplift zone, Sichuan Basin. China Petroleum Exploration 26, 50–67.
Yang, J., Sun, W., Wang, Z., Xue, Y., Tao, I., 1999. Variations in Sr and C isotopes and Ce anomalies in successions from China: evidence for the oxygenation of Neoproterozoic seawater? Precambrian Research 93, 215–233.
Yang, Y., Wen, L., Song, Z., Zhang, B., Yan, W., Zhou, G., Tian, X., Zhong, Y., He, Y., Ma, K., 2022. Breakthrough and potential of natural gas exploration in multi-layer system of Penglai gas area in the north of central Sichuan paleo-uplift. Acta Petrolei Sinica 43, 1351.
You, B., Chen, J., Xiao, H., Fu, R., 2023. Accumulation models and key conditions of crustal-derived helium-rich gas reservoirs. Natural Gas Geoscience 34, 672–683.
Zempolich, W.G., Wilkinson, B.H., Lohmann, K.C., 1988. Diagenesis of late Proterozoic carbonates; the Beck Spring Dolomite of eastern California. Journal of Sedimentary Research 58, 656–672.
Zhang, P., 2019. Origin of Hydrogen sulfide in the Ediacaran and Cambrian in the Central Sichuan Basin. China University of Petroleum (Beijing), Beijing, pp. 68–95.
Zhang, T., Amrani, A., Ellis, G.S., Ma, Q., Tang, Y., 2008. Experimental investigation on thermochemical sulfate reduction by H_2S initiation. Geochimica et Cosmochimica Acta 72, 3518–3530.
Zhang, W., Chen, W., Li, Y., Zhou, J., 2023c. Geochemical characteristics of noble gases in typical helium-rich gas reservoirs and the significance for tracing helium enrichment process. Natural Gas Geoscience 1–20.
Zhang, C., Guan, P., Zhang, J., Song, D., Ren, J., 2023b. Zoning characteristics of helium resources and helium accumulation model in China. Natural Gas Geoscience 34, 656–671.
Zhang, S., He, K., Wang, X., Hu, G., Zhang, B., MIi, J., Su, J., 2021. The multi-path gas generation model and its potential contribution to petroleum accumulation in deep formations. Natural Gas Geoscience 32, 1421–1435.
Zhang, L., Li, J., Xie, Z., Guo, J., Hao, A., Wang, Y., Su, N., Li, J., Li, Z., Chen, D., Zhu, D., 2024. Geochemical characteristics and origin of Sinian-Cambrian natural gas in Penglai Gas area, Sichuan Basin. ACS Omega 9, 23390–23399.
Zhang, B., Zhou, G., Song, Z., Yan, W., Wang, H., Tao, J., Tian, X., Ding, X., Zhong, Y., Ma, K., Yang, D., Li, Y., Zhang, Z., Chen, X., Sun, Y., Xian, Z., Huang, M., 2023a. Multi-layers three-dimensional natural gas accumulation of the Upper Sinian-Lower Cambrian marine carbonate rocks in Penglai gas area, North Slope of central Sichuan paleo-uplift. Marine Origin Petroleum Geology 28, 401–412.
Zhao, W., Li, J., Yang, T., Wang, S., Huang, J., 2016. Geological difference and its significance of marine shale gases in South China. Petroleum Exploration and Development 43, 547–559.
Zhao, W.Z., Xie, Z.Y., Wang, X.M., Shen, A.J., Wei, G.Q., Wang, Z.C., Wang, K., 2021. Sinian gas sources and effectiveness of primary gas-bearing system in Sichuan Basin, SW China. Petroleum Exploration and Development 48, 1260–1270.
Zhu, L., Liu, G., Song, Z., Zhao, W., Tian, X., Dai, X., Wang, Y., Yang, D., Li, Q., Jiang, L., Li, C., Hu, L., 2021. The differences in natural gas from the Dengying Formation in different areas of the north slope of the central Sichuan Paleo-uplift and its controlling factors—Taking Pengtan-1 and Zhongjiang-2 wells as examples. Petroleum Science Bulletin 6, 344–355.
Zhu, L., Liu, G., Song, Z., Benjian, Z., Zhao, W., Tian, X., Ma, K., Wang, Y., Yang, D., Li, Q., Gen, C., Lu, J., 2022. Hydrothermal activity in ultra-deep strata and its geological significance for deep earth gas exploration: Implications from pyrobitumen in the Ediacaran-lower Cambrian Strata, Sichuan Basin. International Journal of Coal Geology 259, 104030.